

# Unexpected fault activation in underground gas storage. Part I: Mathematical model and mechanisms

Andrea Franceschini<sup>a,\*</sup>, Claudia Zoccarato<sup>a</sup>, Selena Baldan<sup>a</sup>, Matteo Frigo<sup>b</sup>, Massimiliano Ferronato<sup>a</sup>, Carlo Janna<sup>a</sup>, Giovanni Isotton<sup>b</sup>, Pietro Teatini<sup>a</sup>

<sup>a</sup>*Department of Civil, Environmental and Architectural Engineering, University of Padova, Padova, 35131 Italy*

<sup>b</sup>*M3E S.r.l., Padova, 35121 Italy*

---

## Abstract

Underground gas storage (UGS) is a worldwide well-established technology that is becoming even more important to cope with seasonal peaks of gas consumption due to the growing uncertainties of the energy market. Safety issues concerning the reactivation of pre-existing faults might arise if the target reservoir is located in a faulted basin, where human activities can trigger (micro-)seismicity events. From a mechanical viewpoint, a fault is activated when the shear stress exceeds the limiting frictional value. In the Netherlands, it has been observed that this occurrence can develop somehow “unexpectedly” after the primary production (PP), i.e., during cushion gas injection (CGI) and UGS cycles, when the stress regime should be in the unloading/reloading path and the fault state far from failure. In order to understand the physical mechanisms responsible for such occurrences and build reliable simulation tools for predictive purposes, a 3D mathematical model coupling frictional contact mechanics in faulted porous rocks with fluid flow is developed, implemented and tested. In particular, the mechanisms and the critical factors responsible for the fault reactivation during the various UGS stages are investigated in the real-world setting of the Rotliegend formation in the Netherlands. The effect of the storage of different fluids for various purposes, such as the long-term sequestration of CO<sub>2</sub>, the regular injection and extraction cycles of CH<sub>4</sub>, and the highly irregular cycles of H<sub>2</sub>, is investigated with respect to fault activation risk. The final aim of this two-part work is to define a safe operational bandwidth for the pore pressure range for UGS activities in the faulted reservoirs of the Rotliegend formation.

Part I of this work concerns the development of the mathematical and numerical model of frictional contact mechanics and flow in faulted porous rocks. A mixed discretization of the governing PDEs under frictional contact constraints along the faults is used, where displacement and pressure in the porous medium, and traction on the fault surfaces are the main variables. A slip-weakening constitutive law governing the fault macroscopic behavior is also presented. The model is tested in the setting of an ideal reservoir located in the Rotliegend formation. The analyses point out how fault reactivation during PP can lead to a stress redistribution, giving rise to a new (deformed) equilibrium configuration. When the fault is reloaded in the opposite direction during the CGI and/or UGS stages, further activation events can occur even if the stress range does not exceed either the undisturbed initial value or the maximum strength ever experienced by the formation.

*Keywords:* Frictional contact, Mixed discretization, Underground gas storage, Slip-weakening law, Fault reactivation

---

## 1. Introduction

Seismicity associated to fluid withdrawal from and injection into deep reservoirs is a geomechanical hazard that is receiving a growing attention in the scientific literature [1, 2, 3]. Fault reactivation, both aseismic and seismic, is caused by the change of the natural stress regime on the discontinuity surface due to the pore pressure  $p$  changes in the reservoir where mining activities are operated. More specifically, the onset and amount of slip, and the size of the

---

\*Corresponding author

*Email address:* andrea.franceschini@unipd.it (Andrea Franceschini)

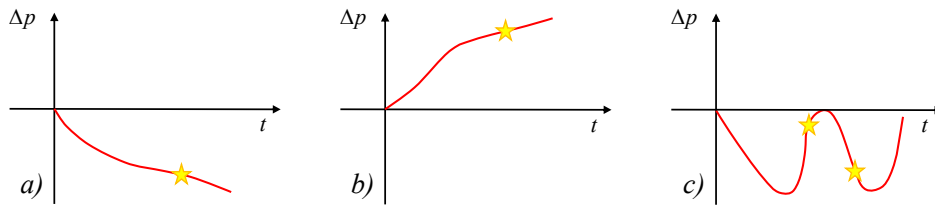


Figure 1: Sketches of two (*a* and *b*) “expected” induced seismicity scenarios and one (*c*) “unexpected”. *a*) Primary production with large pressure drop, *b*) fluid injection (CO<sub>2</sub> sequestration, waste water disposal, fracking) with significant pressure increase), *c*) pressure in the range already experienced (UGS with  $p < p_i$ ).

reactivated fault zone depend on how the stress changes caused by the human operations at depth can interfere with the natural stress regime [4, 5, 6].

The current state-of-the-art research on this topic focuses on the two main processes: i) seismicity induced by production of (conventional) hydrocarbon reservoirs, where pore pressure depletion  $\Delta p$  and differential reservoir compaction are the main factors yielding fault reactivation [4, 7] (Fig. 1a); ii) fluid injection at depth (CO<sub>2</sub> sequestration, production from unconventional reservoirs, enhanced geothermal systems) where, independently of the possible thermal processes, the increase of the fluid pressure (largely) above the natural undisturbed value  $p_i$  within the faulted zone crossing or bounding the targeted formation drives the reactivation of rock discontinuities [8, 9, 10, 11] (Fig. 1b).

Over the last decade, induced seismicity has been observed in some parts of the world also in reservoirs used for underground gas storage (UGS). Somehow unexpectedly, fault reactivation occurred not only during primary production (PP) or gas storage at pressure larger than  $p_i$  [12, 13, 14], i.e., at a stress regime that had never been experienced before by the reservoir and the nearby faults, but also during cushion gas injection (GCI) or producing and storing phases with a pore pressure smaller than  $p_i$  and larger than  $p_{\min}$ , i.e., the minimum pressure experienced by the field usually at the end of primary production before its conversion to UGS (Fig. 1c) [15, 16, 17, 18].

The present work is aimed to shed light on these “unexpected” events. Because of the current CH<sub>4</sub> importance for energy production purposes and the international turbulence on this market, the interest in developing UGS projects is increasing worldwide. Multiple elements presently characterize UGS: seasonal and short-term balancing, strategic reserves in case of interruption of deliveries, optimisation of gas production and gas system distribution, overcoming of local restrictions of gas grids [19, 20]. More recently, UGS has also been investigated as a possible method to store green energy in terms of compressed air and H<sub>2</sub> [21, 22, 23]. Sources of green energy, such as wind, waves, and sun, are characterized by a natural high-frequency fluctuation (from hours to day/night and to weeks). Excess electricity can be used to synthesize hydrogen or to compress air, store the gas in deep aquifers or depleted reservoirs, and use it at a later stage as fuel to generate electricity. The same technology can be also applied for long-term geological sequestration activities, such as CO<sub>2</sub> capture and sequestration to reduce carbon dioxide emissions in the atmosphere [24]. In this case, the targeted reservoir does not undergo a cyclic loading/unloading strength, but the pressure can increase up to a steady state value usually smaller or equal to the initial value  $p_i$ . Analysis of the social and environmental hazards and risks associated with subsurface gas storage is a recurrent issue whenever a new UGS site is planned. Many different aspects are involved, such as formation integrity, health and safety as related to public perception, economic risk, and environmental impact. Among the latter, the geomechanical effects induced by seasonal gas injection and withdrawal, such as movements of the land surface, may play an important role [25].

UGS has been rarely associated with induced seismicity. According to data provided by the European Commission [26], recent works [27], and the *HiQuake* database [28], only a few sites have reported human-induced earthquakes out of 160 UGS facilities in Europe and more than 380 in USA [2]. Three cases of these, i.e., Bergermeer, Norg, and Grijpskerk fields, are located in The Netherlands. These reservoirs are located in the Carboniferous-Rotliegend formation, northern Europe, which is one of the most intensively explored petroleum systems in the world [29], and where a relatively high number of induced seismicity events has been recorded over the last decades [30, 31]. Several studies have addressed the topic of fault reactivation in Rotliegend reservoirs, the most famous of which concerns the Groningen field [32]. Most studies focus on a specific reservoir in the Netherlands and northern Germany, or, more generally, try to investigate the relationship between the typical geological features of these reservoirs, their usual production life, and the possible induced seismicity [7, 33, 34, 35, 6]. The recent literature, however, is mainly

concerned with primary production only and does not investigate the reasons why fault reactivation can occur during UGS phases. Moreover, a very simplified geological structure is assumed in such analyses, with a single fault in a two dimensional (2D) vertical plane, and most likely this can only partially capture the complex response expected from many intersecting faults in a fully three dimensional (3D) environment [34]. Only a few relatively old publications addressed the topic in UGS reservoirs [36, 37]. Nagelhout and Roest [36] developed a 2D geomechanical model by means of the FLAC simulator for a typical faulted vertical section and concluded that *while the gas field is depleted, fault slip occurs due to compaction of the reservoir and due to the upward movement of strata underlying the reservoir. Negligible amounts of additional slip are induced when the reservoir is subjected to alternating injection/extraction periods.* Orlic et al. [37] simulated the geomechanical behavior of a specific UGS reservoir using the finite-element package DIANA. Their results highlighted that *the critically stressed section of the central fault affected by the fault slipped ... during gas production. Additional fault slip could be expected during the subsequent phase of cushion gas injection ... During annual cycles of gas injection and production, the central fault is not critically stressed anymore.*

The aim of this work is multifold: i) to develop a robust computational framework allowing for the simulation of the inception of fault activation in 3D real-world geological settings; ii) to improve the understanding of the physical mechanisms underlying induced seismicity during UGS activities, with specific reference to the typical configurations of Dutch UGS reservoirs; iii) to investigate the factors that can increase the chance of fault reactivation during UGS activities, identifying the settings, conditions and material properties that could most likely cause “unexpected” fault reactivation in the reservoirs located in the Rotliegend formations; iv) to define a set of practical guidelines allowing for a safe operational bandwidth in such UGS fields, in consideration also of the different potential storage activities (CH<sub>4</sub>, H<sub>2</sub>, CO<sub>2</sub>). A few preliminary outcomes were already reported in [38] and [39]. In order to accomplish such a complex multi-disciplinary task, the overall work is subdivided into two parts. The present paper (Part I) is mainly concerned with objectives i) and ii), focusing on the mathematical and computational aspects of the modeling approach, on its application in a representative 3D test case of the problem of interest, and on the mechanisms that can cause “unexpected” fault activation during UGS activities. The application of the model developed herein to the specific real-world cases of the Rotliegend formation, with a detailed sensitivity analysis for the different storage activities and the definition of preliminary guidelines (aforementioned objectives iii) and iv)), is the target of Part II [40].

The paper is organized as follows. The mathematical model of frictional contact mechanics and flow in a 3D visco-elasto-plastic porous medium, built on top of the works [41, 42, 43], is introduced along with its numerical discretization and solution algorithms. Faults are explicitly simulated within the porous rock as inner contact boundaries, whose activation is macroscopically governed by Coulomb’s criterion. Pressure change within the faults, variation of Coulomb’s parameters due to slip-weakening, and the rheology of the caprock are properly accounted for. The model is applied to a synthetic reservoir and fault system that realistically represents the main geological features of the Rotliegend reservoirs. Two scenarios are simulated to deepen the understanding of the geomechanical behavior of a faulted UGS system. Computational results are presented and the mechanisms responsible for fault reactivation during UGS phases are pointed out. A few conclusive remarks close the presentation.

## 2. Mathematical and numerical model

In this section, we discuss the development of the mathematical and numerical model used to investigate the fault activation in the context of UGS reservoirs. The aim is at solving the frictional contact mechanics problem for a faulted porous medium, where the constraints are imposed in an exact way by Lagrange multipliers. The friction behavior of the fracture is governed by Coulomb’s criterion, with a slip-weakening constitutive law. The variational formulation, its numerical discretization and the possible related instability phenomena are discussed. The pore pressure, both in the continuous matrix and inside the fracture network, is computed by a flow simulator with a one-way coupled approach [44, 45], which turns out to be fully warranted at the space and time scale of interest. We use the quasi-static assumption, i.e., no acceleration contribution is accounted for, under the hypothesis of likely negligible inertia of the system when small (e.g., centimetric) slip and small areal extent characterize the fault reactivation [46].

### 2.1. Strong formulation for the contact problem

A fault can be modeled at the macroscale as a lower dimensional internal boundary  $\Gamma_f$  embedded in a 3D domain  $\Omega \subset \mathbb{R}^3$ . The fracture is represented as a pair of surfaces in contact, conventionally denoted as *top* and *bottom*

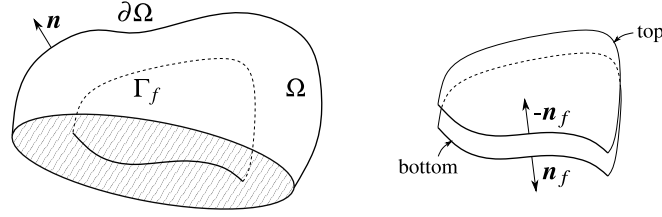


Figure 2: Sketch of the 3D domain  $\Omega$  with its boundary, outer normal and inner fracture  $\Gamma_f$  (left), made of the top and bottom contact surfaces and the normal direction  $\mathbf{n}_f$  (right).

and represented by  $\Gamma_f^+$  and  $\Gamma_f^-$ , respectively. On such surfaces, normal and frictional contact conditions have to be enforced, like the impenetrability of solid bodies and the fulfillment of a friction criterion. In this work, we use Coulomb's frictional criterion to provide the limiting modulus for the shear component of traction on the fault surface. To complete the problem setting definition, we introduce the external domain boundary  $\Gamma \equiv \partial\Omega$ , with its outer unit normal vector  $\mathbf{n}$ , while  $\mathbf{n}_f = \mathbf{n}_f^- = -\mathbf{n}_f^+$  denotes the normal direction to the fracture surface  $\Gamma_f$ . Fig. 2 shows a sketch of the domain  $\Omega$ , the fault  $\Gamma_f$  and the related quantities. Any vector field can be decomposed along the normal and tangential direction to the fracture, i.e.,  $\mathbf{v} = v_N \mathbf{n}_f + \mathbf{v}_T$ , with  $v_N = \mathbf{n}_f^T \mathbf{v}$  and  $\mathbf{v}_T = \mathbf{v} - v_N \mathbf{n}_f = (\mathbf{1} - \mathbf{n}_f \otimes \mathbf{n}_f) \mathbf{v}$ , where the subscripts  $N$  and  $T$  are used to denote the normal and tangential components, respectively, and  $\mathbf{1}$  is the identity tensor of order 2.

Assuming quasi-static conditions and infinitesimal strains, the strong form of the linear momentum balance at every instant  $t$  in the time interval  $[0, t_{\max}]$  can be stated as follows [47, 48, 49]: find the displacement vector  $\mathbf{u} : \bar{\Omega} \times [0, t_{\max}] \rightarrow \mathbb{R}^3$  such that:

$$\nabla \cdot \hat{\boldsymbol{\sigma}}(\mathbf{u}) + \mathbf{b} = 0 \quad \text{in } \Omega \times [0, t_{\max}], \quad (1a)$$

$$\mathbf{u} = \bar{\mathbf{u}} \quad \text{on } \Gamma_u \times [0, t_{\max}], \quad (1b)$$

$$\hat{\boldsymbol{\sigma}}(\mathbf{u}) \cdot \mathbf{n} = \bar{\mathbf{t}} \quad \text{on } \Gamma_\sigma \times [0, t_{\max}], \quad (1c)$$

where  $\hat{\boldsymbol{\sigma}}$  is the total stress tensor,  $\mathbf{b}$  collects the external body loads and  $\Gamma_u \cup \Gamma_\sigma = \Gamma$ ,  $\Gamma_u \cap \Gamma_\sigma = \emptyset$ , are the portion of the boundary where Dirichlet and Neumann conditions are imposed, respectively. On the fracture  $\Gamma_f$ , normal and friction compatibility conditions need to be enforced [48, 49]. The normal contact conditions on the fracture read:

$$t_N = \mathbf{t} \cdot \mathbf{n}_f \leq 0 \quad \text{only compressive traction is allowed,} \quad (2a)$$

$$g_N = \llbracket \mathbf{u} \rrbracket \cdot \mathbf{n}_f \geq 0 \quad \text{impenetrability condition,} \quad (2b)$$

$$t_N g_N = 0 \quad \text{either the fracture is compressed or it is open.} \quad (2c)$$

The conditions for the frictional component are:

$$\|\mathbf{t}_T\|_2 \leq \tau_{\max}(t_N, \|\mathbf{g}_T\|_2) \quad \text{Coulomb's criterion,} \quad (3a)$$

$$\dot{\mathbf{g}}_T \cdot \mathbf{t}_T - \tau_{\max}(t_N, \|\mathbf{g}_T\|_2) \|\dot{\mathbf{g}}_T\|_2 = 0 \quad \text{frictional traction is aligned with sliding rate.} \quad (3b)$$

In Eqs. (2)-(3), we split the traction  $\mathbf{t}$  on the fracture and the displacement jump across it into normal and tangential components, i.e.,  $\mathbf{t} = t_N \mathbf{n}_f + \mathbf{t}_T$  and  $\llbracket \mathbf{u} \rrbracket = g_N \mathbf{n}_f + \mathbf{g}_T$ , respectively. The jump is defined as  $\llbracket \mathbf{u} \rrbracket = \mathbf{u}|_{\text{top}} - \mathbf{u}|_{\text{bottom}}$ . To characterize the standard Coulomb frictional criterion,  $c$  and  $\varphi$  are introduced, i.e., the cohesion and the friction angle, respectively, obtaining:

$$\tau_{\max}(t_N, \|\mathbf{g}_T\|_2) = c - t_N \tan(\varphi(\|\mathbf{g}_T\|_2)). \quad (4)$$

In Eq. (4), the friction angle generally depends on the modulus of the tangential component of the displacement jump, i.e., the slippage, so as to simulate a slip-weakening frictional behavior. Since a quasi-static approach is used, we can replace the tangential displacement rate  $\dot{\mathbf{g}}_T$  in Eq. (3b) with the incremental tangential displacement  $\Delta \mathbf{g}_T$  with respect to the previous time-step value [50].

The fault surface  $\Gamma_f$  can be split into three non-intersecting portions. Each portion is characterized by a different operating mode allowed for by the possible combinations of the previous conditions (2)-(3):

- *Stick*: the surface is compressed ( $t_N < 0$ ) and the shear traction modulus does not exceed the limiting value provided by the criterion in Eq. (4). The displacement field is continuous across  $\Gamma_f$ ;
- *Slip*: the normal traction is still negative, but the surface is free to slip. In this case, Coulomb's equality holds [51]:

$$\mathbf{t}_T^* = \tau_{\max}(t_N, \|\mathbf{g}_T\|_2) \frac{\Delta \mathbf{g}_T}{\|\Delta \mathbf{g}_T\|_2}. \quad (5)$$

Only the normal component of the displacement field is continuous across  $\Gamma_f$ ;

- *Open*: the normal traction is non-negative and the two contact surfaces  $\Gamma_f^+$  and  $\Gamma_f^-$  are free to move on condition to avoid compenentration. Hence, the displacement field across  $\Gamma_f$  is discontinuous and the traction on the fault vanishes, i.e.,  $\mathbf{t} = 0$ .

For additional details on the mathematical formulation, see [47, 48, 49] and more recently [41, 52, 53].

According to Terzaghi's principle, the total stress tensor in a saturated porous medium can be decomposed as the sum of two contributions: the effective stress tensor acting on the solid skeleton and a volumetric term depending on the averaged fluid pressure  $p$ :

$$\hat{\boldsymbol{\sigma}} = \begin{cases} \boldsymbol{\sigma} - \mathbf{1}p & \text{on } \Gamma_\sigma \cup \Gamma_f, \\ \boldsymbol{\sigma} - \alpha \mathbf{1}p = \mathbb{C} : \boldsymbol{\varepsilon} - \alpha \mathbf{1}p & \text{in } \Omega, \end{cases} \quad (6)$$

where the fluid pressure is averaged by the saturation indices of the different phases,  $\alpha$  is the Biot coefficient, taking care of the ratio between the grain and the porous matrix compressibility, and  $\mathbf{1}$  the identity tensor of order 2 [54]. The effective stress tensor  $\boldsymbol{\sigma}$  is called effective Terzaghi stress tensor on the domain boundaries, while it is the effective Biot stress tensor inside the domain itself. In Eq. (6), the constitutive relationship defining the effective Biot stress tensor is introduced, where  $\mathbb{C}$  is a fourth order elasticity tensor, generally non-linear, and  $\boldsymbol{\varepsilon} = \nabla^s \mathbf{u}$  is the strain tensor, with  $\nabla^s = (\nabla + \nabla^T)/2$  the symmetric gradient operator. The mechanical constitutive law relates a strain variation in the porous medium to an effective stress variation. Such a law can be described by a simple linear elastic model (Hooke's law), with constant or variable parameters, but also more complex elasto-plastic rules with time-dependent contributions can be introduced, e.g., a visco-elasto-plastic law. For more details on the appropriate constitutive laws and their implementations, see [51, 55].

## 2.2. Mass balance equation

The mass conservation of the fluid species  $\kappa$  reads [56, 57, 58, 59]:

$$\frac{\partial}{\partial t}(\rho^\kappa) + \nabla \cdot \mathbf{F}^\kappa = q_s^\kappa, \quad (7)$$

where  $\rho^\kappa$  and  $\mathbf{F}^\kappa$  are the density and the flux, respectively, of the fluid species  $\kappa$ . The density  $\rho^\kappa$  represents the mass of  $\kappa$  per unit of rock volume and can be written as:

$$\rho^\kappa = \phi \sum_{\beta} S_{\beta} \rho_{\beta} \chi_{\beta}^{\kappa}, \quad (8)$$

with  $\phi$  the porosity,  $S_{\beta}$  the saturation of phase  $\beta$ , that can be either liquid or gas,  $\rho_{\beta}$  the density of phase  $\beta$ , and  $\chi_{\beta}^{\kappa}$  the mass fraction of component  $\kappa$  in phase  $\beta$ . Usually, assuming isothermal conditions the fluid density is a function of pressure, but can also depends on other quantities, such as the mass fraction according to some equation of state. Saturations and mass fractions are constrained by the well-known conditions:

$$\sum_{\beta} S_{\beta} = 1 \quad \text{and} \quad \sum_{\kappa} \chi_{\beta}^{\kappa} = 1. \quad (9)$$

The fluid flux of component  $\kappa$  is the sum of the fluxes for each phase:

$$\mathbf{F}^\kappa = \sum_{\beta} \chi_{\beta}^{\kappa} \mathbf{F}_{\beta}, \quad (10)$$

and each phase flux is described by Darcy's law as:

$$\mathbf{F}_\beta = \rho_\beta \mathbf{v}_\beta = -\rho_\beta \frac{\mathbf{k} k_{r,\beta}}{\mu_\beta} (\nabla p_\beta - \rho_\beta \mathbf{g}), \quad (11)$$

with  $\mu_f$  and  $k_{r,\beta}$  the viscosity and the relative permeability of the phase,  $\mathbf{k}$  the permeability tensor, and  $p_\beta$  the pressure in phase  $\beta$ .

According to [54, 60], the porosity update accounting for poro-elastic effects can be expressed as:

$$\phi = \phi_0 + \alpha \varepsilon_v + \frac{(\alpha - \phi_0)(1 - \alpha)}{K_d} (p - p_0), \quad (12)$$

where  $K_d$  is the drained bulk modulus,  $\varepsilon_v = \text{trace}(\boldsymbol{\varepsilon})$  is the volumetric strain, and  $\phi_0$  and  $p_0$  are the reference porosity and fluid pressure respectively. In Eq. (12),  $p$  is the averaged fluid pressure, computed as:

$$p = \sum_{\beta} S_{\beta} p_{\beta}. \quad (13)$$

In oedometric conditions and a constant total stress state, from Terzaghi's principle (Eq. (6)) we have  $d\sigma_z = \alpha dp$  and

$$\frac{\partial}{\partial t} \varepsilon_v = C_m \alpha \frac{\partial}{\partial t} p, \quad (14)$$

with  $C_m$  is the vertical uniaxial compressibility. In this case, the mass balance is decoupled from the linear momentum balance and can be solved in advance, providing a pressure field acting as an external body load for the structural problem. Even though this assumption is not guaranteed for the reservoir application considered in the present work, at the (large) space and time scale of interest coupling is weak and a one-way coupled approach, where Eqs. (7) are solved first for all the fluid species and the averaged pressure of Eq. (13) is then introduced into Eq. (1), is fully warranted, see for instance [44, 61, 62, 63, 64, 65].

The set of Eqs. (7) for obtaining the pressure field in the porous medium is usually solved applying a finite volume method because it preserves the mass conservation at the elemental level [66, 67, 68]. Nevertheless, also a finite element or mixed finite element approach can be successfully used, e.g., [69, 70, 71, 72, 73]. In our analysis, the numerical simulation of the multiphase flow in the porous matrix has been carried out by using *Open Porous Media*, an open-source reservoir simulator based on a classical finite volume discretization [74, 75]. As to the computation of the pressure field within the network of faults, two strategies can be employed: either the domain explicitly contains the faults as *thin* 3D cells, or the pressure is extended to the faults from the surrounding 3D cells, according to some physical treatment of the contact surfaces as inner boundaries. We elect to use the latter approach, thus allowing to represent the fault at the macroscale as zero-thickness lower dimensional elements. Generally speaking, the two limiting cases that can be met in reality are *sealing* and *non-sealing* faults. In the former case, the fault acts as an impermeable barrier and the pressure change does not propagate from one side to the other of the contact surfaces. In this situation, we can assume that the pressure variation in the fault is null. On the contrary, in the latter case, the fault is fully permeable and does not exhibit any resistance to the fluid flow. In this situation, we assume the pressure variation in the fault to be equal to the arithmetic average of the pressure computed on the two side cells.

### 2.3. Variational formulation and discretization

In this section, the variational formulation for the strong form of the linear momentum balance in Eq. (1), equipped with the constraints of Eqs. (2)-(3), is presented.

The weak form of the governing equations naturally produces a variational inequality because of the frictional contact constraints [47]. In order to avoid this difficulty, it is possible to reduce the original inequality to a standard variational formulation by an active-set strategy and either a penalty regularization or the introduction of Lagrange multipliers. We elect to use the Lagrange multiplier technique, which can be computationally more expensive, because new primary unknowns are introduced and the resulting algebraic problem gains a saddle-point nature, but generally much more accurate, robust and stable. Moreover, though generating saddle-point systems, this formulation

allows to produce a sequence of linear problems less sensible to ill-conditioning issues [76]. From a physical viewpoint, Lagrange multipliers represent the traction field on the fault surfaces, thus the stress evaluation and the related reactivation risk becomes straightforward.

We emphasize that to retrieve the complete variational formulation for the problem at hand, defining the right functional spaces and conditions, is far beyond the purposes of this work and we refer the interested readers to more specific researches, like Kikuchi and Oden [47] and Wohlmuth [50]. Here, we briefly report the selected function spaces and the residual equations. The notations  $(\cdot, \cdot)_\Omega$  and  $\langle \cdot, \cdot \rangle_\Gamma$  denote the  $L^2$ -inner product of functions in  $\Omega$  (3D domain) and  $\Gamma$  (lower dimensional domain), respectively. Let  $\mathcal{V} = [H^1(\Omega)]^3$  be the Sobolev space of vector functions whose first derivatives belong to  $L^2(\Omega)$ ; let  $\mathcal{M}$  be the dual space of the trace space  $\mathcal{W} = [H^{1/2}(\Omega)]^3$ ; and let  $\mathcal{M}(t_N, \|\mathbf{g}_T\|)$  be its subspace such that

$$\mathcal{M}(t_N, \|\mathbf{g}_T\|) = \left\{ \boldsymbol{\mu} \in \mathcal{M} : \langle \boldsymbol{\mu}, \mathbf{v} \rangle_{\Gamma_f} \leq \langle \tau_{\max}(t_N, \|\mathbf{g}_T\|_2), \|\mathbf{v}_T\|_{\Gamma_f}, \mathbf{v} \in \mathcal{W} \text{ with } v_N \leq 0 \right\}. \quad (15)$$

Given the finite-dimensional subspaces  $\mathcal{V}^h \subset \mathcal{V}$  and  $\mathcal{M}^h(t_N^h, \|\mathbf{g}_T^h\|) \subset \mathcal{M}(t_N, \|\mathbf{g}_T\|)$ , the finite dimensional weak form of the problem in Eq. (1) with Terzaghi relation of Eq. (6) and conditions Eqs. (2)-(3) can be stated as follows: at every instant  $t \in [0, t_{\max}]$ , find  $\{\mathbf{u}^h, \mathbf{t}^h\} \in \mathcal{V}^h \times \mathcal{M}^h(t_N^h, \|\mathbf{g}_T^h\|)$  such that:

$$\begin{aligned} \mathcal{R}_u &= (\nabla^s \boldsymbol{\eta}, \hat{\boldsymbol{\sigma}})_\Omega - \langle \boldsymbol{\eta}, \hat{\boldsymbol{\sigma}} \cdot \mathbf{n} \rangle_\Gamma - (\boldsymbol{\eta}, \mathbf{b})_\Omega \\ &= (\nabla^s \boldsymbol{\eta}, \hat{\boldsymbol{\sigma}})_\Omega - \langle \boldsymbol{\eta}, \hat{\boldsymbol{\sigma}} \cdot \mathbf{n}_f^+ \rangle_{\Gamma_f^+} - \langle \boldsymbol{\eta}, \hat{\boldsymbol{\sigma}} \cdot \mathbf{n}_f^- \rangle_{\Gamma_f^-} - \langle \boldsymbol{\eta}, \hat{\boldsymbol{\sigma}} \cdot \mathbf{n} \rangle_{\Gamma_\sigma} - (\boldsymbol{\eta}, \mathbf{b})_\Omega \\ &= \left( \nabla^s \boldsymbol{\eta}, \boldsymbol{\sigma}(\mathbf{u}^h) - \alpha \mathbf{1}p \right)_\Omega - \langle \llbracket \boldsymbol{\eta} \rrbracket, \mathbf{t}^h - p \mathbf{n}_f \rangle_{\Gamma_f} - \langle \boldsymbol{\eta}, \bar{\mathbf{t}} \rangle_{\Gamma_\sigma} - (\boldsymbol{\eta}, \mathbf{b})_\Omega = 0 \quad \forall \boldsymbol{\eta} \in \mathcal{V}^h, \end{aligned} \quad (16a)$$

$$\mathcal{R}_t = \langle \mathbf{t}_N^h - \boldsymbol{\mu}, \mathbf{g}_N \rangle_{\Gamma_f} + \langle \mathbf{t}_T^h - \boldsymbol{\mu}_T, \Delta \mathbf{g}_T \rangle_{\Gamma_f} \geq 0 \quad \forall \boldsymbol{\mu} \in \mathcal{M}^h(t_N^h, \|\mathbf{g}_T^h\|). \quad (16b)$$

We use a Galerkin approach, hence the test functions  $\boldsymbol{\eta}$  and  $\boldsymbol{\mu}$  belong to the same function spaces used to define the trial functions for the displacement and traction field, respectively. To transform the variational inequality of Eq. (16b) into a variational equality, an iterative active-set algorithm [77, 78] is applied. According to this approach, the fault surfaces  $\Gamma_f$  is subdivided into active and inactive regions for both components of the traction, i.e., the *Stick* ( $\Gamma_f^{\text{stick}}$ , active for normal and tangential components), *Slip* ( $\Gamma_f^{\text{slip}}$ , active for normal component), and *Open* ( $\Gamma_f^{\text{open}}$ , inactive) portions of  $\Gamma_f$ . With this subdivision, the variational inequality of Eq. (16b) becomes:

$$\mathcal{R}_t = \langle \boldsymbol{\mu}, \llbracket \mathbf{u}^h \rrbracket \rangle_{\Gamma_f^{\text{stick}}} + \langle \boldsymbol{\mu}_N, \mathbf{g}_N \rangle_{\Gamma_f^{\text{slip}}} + \frac{1}{k} \langle \boldsymbol{\mu}_T, \mathbf{t}_T^h - \mathbf{t}_T^* \rangle_{\Gamma_f^{\text{slip}}} + \frac{1}{k} \langle \boldsymbol{\mu}, \mathbf{t}^h \rangle_{\Gamma_f^{\text{open}}} = 0 \quad \forall \boldsymbol{\mu} \in \mathcal{M}^h(t_N^h, \|\mathbf{g}_T^h\|), \quad (17)$$

where  $k$  is a unitary coefficient introduced to ensure dimensional consistency. The non-linear system of Eqs. (16a)-(17) is solved by a Newton linearization and at convergence we check the consistency of the traction state on the faults with the initial subdivision of  $\Gamma_f$  into  $\Gamma_f^{\text{stick}}$ ,  $\Gamma_f^{\text{slip}}$ , and  $\Gamma_f^{\text{open}}$ . If the consistency check is satisfied, the active-set algorithm is stopped and we can move to the following time instant, otherwise a new subdivision of  $\Gamma_f$  is defined, Eq. (17) is re-computed and the resulting non-linear system solved again.

Introducing  $\mathbf{u}^h = \sum_i u_i \boldsymbol{\eta}_i$  and  $\mathbf{t}^h = \sum_j t_j \boldsymbol{\mu}_j$ , i.e., the discrete representation of the displacement and traction fields, where  $\{\boldsymbol{\eta}_i\}$  and  $\{\boldsymbol{\mu}_j\}$  are bases for  $\mathcal{V}^h$  and  $\mathcal{M}^h(t_N^h, \|\mathbf{g}_T^h\|)$ , respectively, the set of variational equalities of Eqs. (16a)-(17) becomes an algebraic nonlinear system. The bases for the finite-dimensional spaces  $\mathcal{V}^h$  and  $\mathcal{M}^h$  are selected with the aid of the finite element method. Given the regularity requirements defined above, we use low-order discretization spaces for both displacement and traction. The computational domain is subdivided into non-overlapping hexahedral elements,  $\Omega = \bigcup_{i=1}^{n_e} \Omega_i$  and  $\Omega_i \cap \Omega_j = \emptyset$  for any  $i \neq j$ . This choice is done for the sake of the consistency with the domain discretization used for the multiphase flow model, which is based on a standard finite volume approach. We use a conformal representation of the faults, i.e.,  $\Gamma_f = \bigcup_j \partial \Omega_j$ , where  $\Omega_j$  are elements sharing a face with  $\Gamma_f$ . In such a way, the fault contact surfaces are composed by pairs of quadrilateral elements. Each pair of quadrilateral elements is also denoted as a zero-thickness *interface finite element* [79]. According to the value of the traction, every interface element can change its status, i.e., it can belong to either the stick, slip or open portion of  $\Gamma_f$ .

The mixed finite element discretization adopted in this work is described in Franceschini et al. [52, 53]. It consists of a  $\mathbb{Q}_1$  first-order interpolation for the nodal-based displacement field and a  $\mathbb{P}_0$  piecewise constant interpolation for the element-based traction field. The collection of coefficients  $u_i$  and  $t_j$  are the components of the unknown algebraic

arrays, named  $\mathbf{u}$  and  $\mathbf{t}$  of sizes  $3n_n$  and  $3n_f$ , with  $n_n$  the number of nodes in the hexahedral mesh and  $n_f$  the number of interface elements. This approach has the main advantage of being naturally coupled with a finite volume pressure solution computed on the same domain discretization at no additional cost, since both the traction and the pressure are represented using the same space on the same grid. On the other side, in order to ensure the LBB-stability of the proposed mixed finite element spaces, a tailored jump stabilization has been proposed in [53]. For a complete analysis of the LBB-stability of a general pair of mixed finite element spaces, see Elman et al. [80]. An implementation of the presented algorithm can be found in [81].

We emphasize that even if a linear elastic constitutive relation is used for the porous medium, the set of equations reported in Eqs. (16a)-(17) represents a non linear problem, because a consistent partitioning of the fracture surface is unknown and has to be computed depending on the solution vectors. To be more specific, constraints in Eqs. (2)-(3) are the Karush-Kuhn-Tucker (KKT) conditions and we are dealing with a non-linear optimization problem [77]. As already mentioned, the solution strategy is based on an active-set strategy, with each non-linear problem addressed by a classical exact Newton algorithm.

#### 2.4. Linearization and linear system solution

The use of a mixed finite element approximation produces a linearized step with a generalized saddle-point Jacobian matrix [82]. The Jacobian is generally non-symmetric because of the contribution related to the friction component of the traction when the fracture slides. In particular, at each Newton iteration, the linear system that has to be solved is:

$$J\delta\mathbf{x} = -\mathbf{r}, \quad (18)$$

with the  $2 \times 2$  block matrix  $J$ , the residual vector  $\mathbf{r}$ , and the solution vector  $\delta\mathbf{x}$  given by:

$$J = \begin{bmatrix} \frac{\partial \mathcal{R}_u}{\partial \mathbf{u}} & \frac{\partial \mathcal{R}_u}{\partial \mathbf{t}} \\ \frac{\partial \mathcal{R}_t}{\partial \mathbf{u}} & \frac{\partial \mathcal{R}_t}{\partial \mathbf{t}} \end{bmatrix}, \quad \mathbf{r} = \begin{bmatrix} \mathcal{R}_u \\ \mathcal{R}_t \end{bmatrix}, \quad \text{and} \quad \delta\mathbf{x} = \begin{bmatrix} \delta\mathbf{u} \\ \delta\mathbf{t} \end{bmatrix}, \quad (19)$$

where  $\mathcal{R}_u$  and  $\mathcal{R}_t$  are computed at the current counter level  $l$ . As usual, the updated solution vector at level  $l+1$  is:

$$\begin{bmatrix} \mathbf{u} \\ \mathbf{t} \end{bmatrix}^{l+1} = \begin{bmatrix} \mathbf{u} \\ \mathbf{t} \end{bmatrix}^l + \begin{bmatrix} \delta\mathbf{u} \\ \delta\mathbf{t} \end{bmatrix}. \quad (20)$$

For the detailed expression of the Jacobian, see [52]. The resulting linear system is characterized by a large and sparse matrix and it is necessary to use a preconditioned iterative method for its efficient solution. To achieve satisfactory results, the use of a suitable preconditioner is mandatory. Since the properties of the linear system may change significantly as the simulation proceeds and the fault elements change status, also the preconditioner must evolve. Among others, an idea is to exploit the scalability intrinsically present in the multigrid approach and combine it with the known physics-based partitioning of the blocks to be able to solve the saddle-point matrix. For details on robust and efficient techniques used for the solution of this peculiar linear system, the reader may refer to [42, 53, 83].

#### 2.5. Constitutive model for fracture: slip weakening

In this work we use both the classical Coulomb criterion with a constant friction coefficient, and a slip-weakening friction law with a variable friction coefficient. Originally used by Andrews [84] to take into account the change from static to dynamic friction, slip-weakening friction laws [85, 86] are based on the concept that the shear stiffness of the fracture decreases as sliding occurs. From a mathematical viewpoint, the standard Coulomb criterion reads:

$$\|\mathbf{t}_T\|_2 \leq c - t_N\mu, \quad \text{with } \mu = \tan \varphi, \quad (21)$$

while a more general slip-weakening friction law reads:

$$\|\mathbf{t}_T\|_2 \leq c - t_N\mu(\|\mathbf{g}_T\|_2). \quad (22)$$

A simple expression to account for the friction reduction with fault motion is provided by a piecewise linear function, as shown in Fig. 3, where the friction coefficient linearly decreases from the static value  $\mu_s$  down to the dynamic



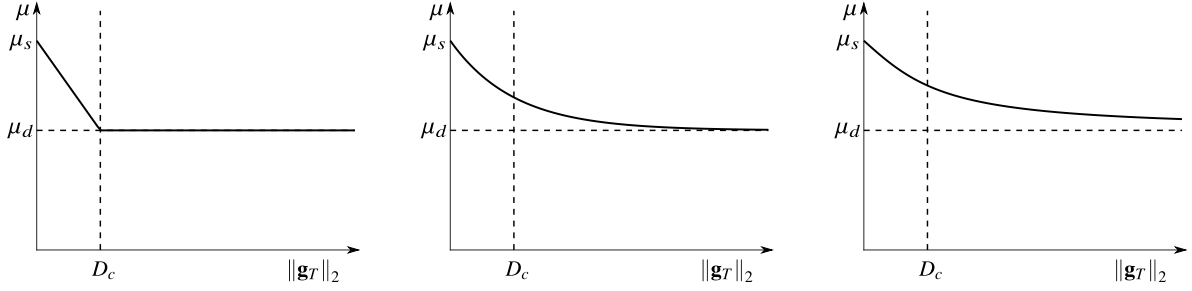


Figure 3: Slip weakening constitutive laws. From left to right: piecewise linear friction law, exponential friction law and inverse trigonometric friction law.

value  $\mu_d$  at a sliding value equal to  $D_c$ . For larger sliding values, the friction coefficient remains constantly equal to  $\mu_d$ . Other analytical expression can be also used to simulate the friction coefficient reduction with the sliding, such as an exponential law (see Fig. 3), which has the advantage to allow for a *smooth* variation that can be differentiated everywhere. It provides:

$$\mu = \mu_d + (\mu_s - \mu_d) \exp\left(-\frac{\|g_T\|_2}{D_c}\right). \quad (23)$$

A similar smooth behavior can be formulated based on inverse trigonometric functions (see Fig. 3):

$$\mu = \mu_d + (\mu_s - \mu_d) \left(1 - \frac{2}{\pi} \arctan \frac{\|g_T\|_2}{D_c}\right). \quad (24)$$

In order to compare the three different expressions, we use the simple 1D problem sketched in Fig. 4. The selected physical parameter set is:  $\mu_s = \tan(30^\circ)$ ,  $\mu_d = \tan(10^\circ)$ ,  $D_c = 2$  mm, with the spring stiffness  $K = 11 \times 10^9$  N/m and a compression load  $N = 3 \times 10^7$  N. The first three values are representative of the conditions typically found in the seismogenic gas fields within the Rotliegend stratigraphic units in the Netherlands [45, 87]. The physical quantities of interest are shown in Fig. 4. The primary variable is always the displacement of the point where the external load  $N$  is applied, while the outcomes are: (i) the friction strength  $F$ , (ii) the relative displacement  $u_r$  between the body connected to the spring and the fixed basement, (iii) the global system stiffness  $\bar{K}$ , and (iv) the internal energy  $U$ . Though the response in terms of friction strength are different, both relative displacement and global energy are comparable. By distinction, the global stiffness behaves differently and for two cases out of three it reaches negative amounts that are greater in absolute value than the original spring stiffness  $K$ . The finite element approach used in the present modeling analysis is based on the global equilibrium of the system and not on a local (elemental) balance. This is the reason why a comparison of the global energy associated with the different laws is meaningful. At the elemental level, it is desirable to avoid negative stiffness, which could potentially lead to friction instabilities. Hence, we chose to work with the law based on the inverse trigonometric function, i.e., the only providing a minimum stiffness smaller in absolute value than the original one. In such a way, we can ensure, at least for conditions similar to the ones used in this example, a positive global stiffness.

### 3. Model set-up

#### 3.1. Conceptual model

In order to test the mathematical model and identify the main mechanisms governing fault reactivation in UGS fields, we use a simplified geological model representative of the typical features of the Rotliegend UGS reservoirs, such as Norg and Grikpskerk [18], e.g., see Fig. 5. These reservoirs are bounded by normal faults with a significant throw (up to a 250 m) and consist of a few compartments separated by internal faults. The gas fields are located between 2000 and 3000 m of depth, with the Rotliegend reservoir rock characterized by an average net thickness of

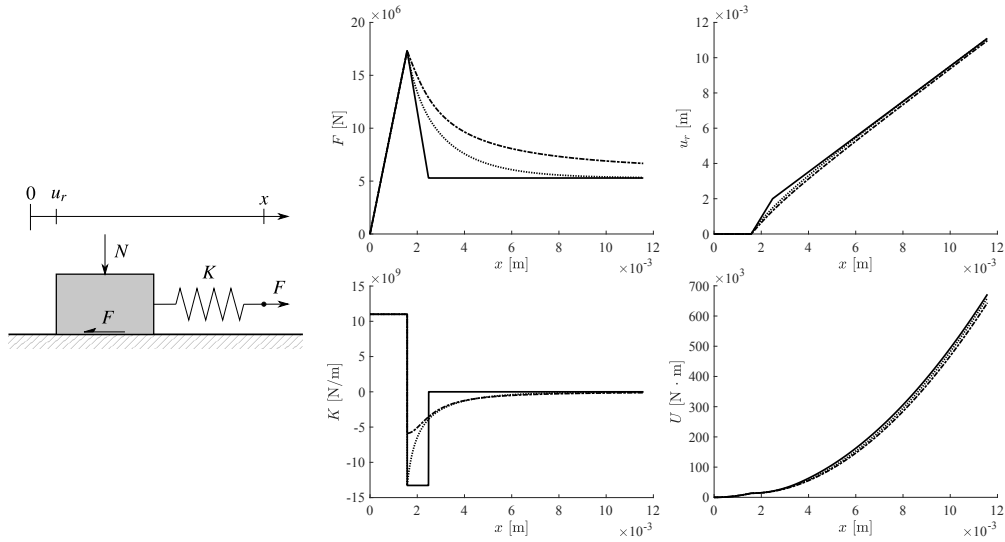


Figure 4: Mono-dimensional friction system with 1 degree of freedom. On the left: sketch of the model used in this example. On the right, from the top left, (i) friction strength, (ii) relative displacement, (iii) global system stiffness and (iv) internal energy. Continuous, dotted and dashed line represent linear, exponential and inverse trigonometric slip-weakening formulation, respectively

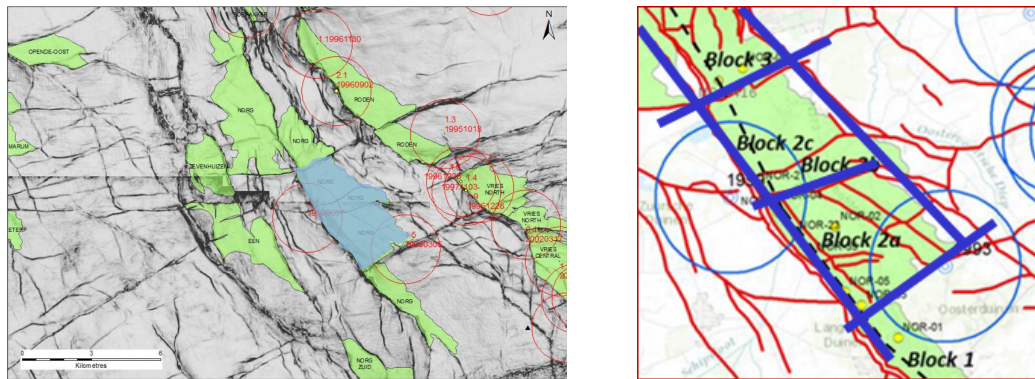


Figure 5: On the left: base Zechstein semblance map of the Norg UGS (in blue) and surrounding area with traces of the bounding faults and localization of the recorded seismic events. On the right: conceptual map of the Norg field with major and minor faults highlighted in blue and red, respectively.

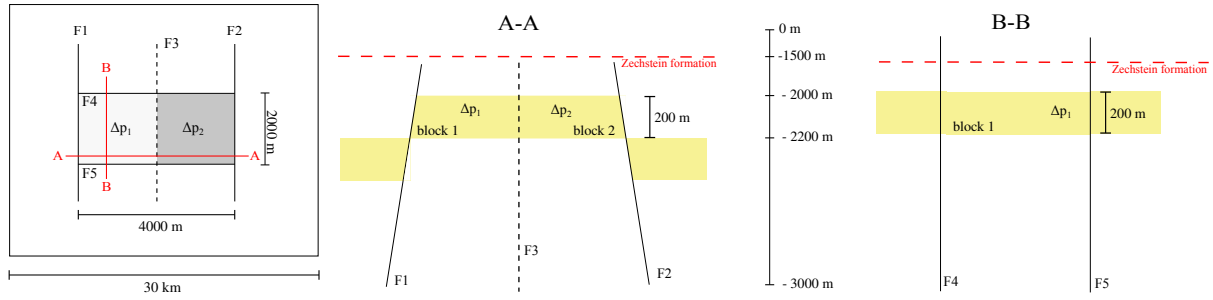


Figure 6: On the left: plain view of the model. On the right: vertical sections of the conceptual model along the trace A-A and B-B shown on the left.

150-200 m. Detailed information about the geological setting and typical geometric features of UGS reservoirs in the Netherlands can be found, among others, in [16, 37, 88, 89] and published reports [17, 18].

Based on those features, we define a conceptual model composed of two adjacent compartments, 2000×2000 m wide, 200 m thick, and 2000 m deep, where UGS activities are carried out. The reservoir compartments are laterally confined by two families of orthogonal faults, denoted as F1-F2 (parallel to y-axis) and F4-F5 (parallel to x-axis). Another fault, denoted as F3, separates the two reservoir blocks (Fig. 6). The two compartments have only a partial hydraulic connection depending on the sealing properties of fault F3, so the pore pressure distribution in space and time may be different. Faults F1 and F2 are inclined with respect to the vertical z-axis by a dip angle equal to  $\pm 10^\circ$ , while F3, F4 and F5 are vertical faults, as shown in Fig. 6. The faults extend from -3000 m to -1600 m depth, i.e., they terminate within the caprock sealing the reservoir, called Zechstein formation. Notice that the blocks have a 200-m offset along the vertical direction, corresponding to the entire thickness of the reservoir, relative to the Rotliegend formation located in the sideburden.

### 3.2. Finite element-interface element discretization

The reservoir is embedded in a 30-km wide square domain. The overall model size is much larger than the reservoir dimension to minimize the effects of the (arbitrary) boundary conditions on the solution in the area of interest (Fig. 6). The bottom of the model is 5000-m deep and the land surface is located at the elevation of 0 m. Standard conditions with zero displacement and zero pore pressure variation on the outer and bottom boundaries are prescribed, whereas the land surface is a traction-free boundary.

A 3D finite element mesh of the selected domain is built by using hexahedral elements, which are particularly suitable for the symmetric configuration with the faults parallel to the Cartesian axes. Fig. 7 shows an axonometric view of the full computational grid used in the geomechanical model. The mesh consists of 253,165 nodes and 236,208 hexahedral elements with a finer discretization in the reservoir layers, i.e., at depth between 2000 and 2200 m. The element size within the reservoir is 100×100×20 m. Fig. 8 shows the fault system embedded in the continuous 3D grid as discretized by 5,215 interface elements. The state of each element of the faults is synthetically evaluated with the aid of the *criticality index* defined as:

$$\chi = \frac{\|t_T\|_2}{\tau_{\max}} = \frac{\|t_T\|_2}{c - t_N \tan(\varphi(\|g_T\|_2))}. \quad (25)$$

From Eq. (25), it is easy to see that  $\chi \in [0, 1]$ , where 0 is associated with the safest condition and 1 to plastic sliding.

### 3.3. Simulated scenarios

To evaluate the capabilities of the presented numerical model and understand the possible mechanisms causing fault reactivation during CGI and UGS, a few scenarios are simulated in the typical setting of the Rotliegend reservoirs in the Netherlands. The main geological and geomechanical parameters are reported in Tab. 1. For the sake of simplicity, a linear elastic behavior is assumed in the reservoir during the UGS activities.

The pressure history prescribed in an active well located in each compartment is sketched in the leftmost frame of Fig. 9. We assume a 10-y duration for the PP phase, where the pressure drops linearly by up to 20 MPa. After this

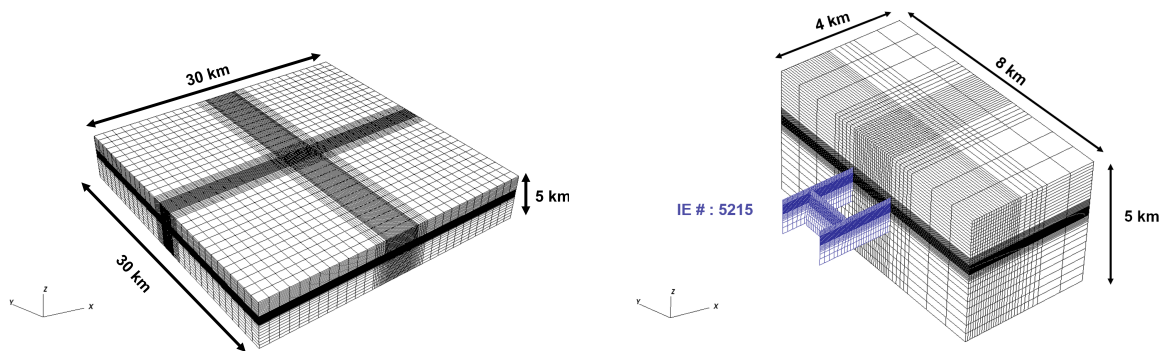


Figure 7: Axonometric view of the computational domain used for the geomechanical simulations: full 3D finite element grid (left) and interface element grid (blue) embedded in a portion of the full 3D grid (right).

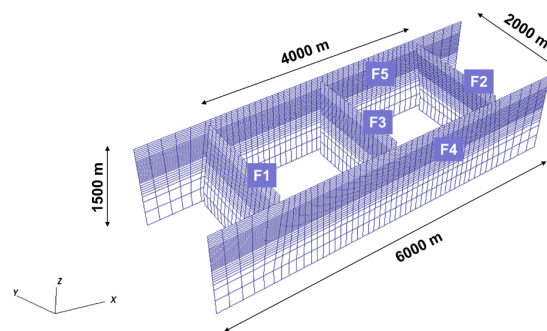


Figure 8: Interface element discretization of the fault discontinuities. The planar trace of F1, F2 and F3 is parallel to the  $y$ -axis, whereas that of F4 and F5 is parallel to the  $x$ -axis. F3 is the central fault separating the two reservoir compartments.

Table 1: Formation-dependent geomechanical parameters. See Fig. 6 for a detail on the depths.

layer	density [kg/m <sup>3</sup> ]	Young modulus [GPa]	Poisson ratio
Overburden	2200	10.0	0.25
Upper Zechstein Salt (-1500 to -1800 m)	2100	35.0	0.30
Lower Zechstein Salt (below -1800 m)	2100	20.0	0.30
Reservoir (Upper Rotliegend)	2400	11.0	0.15
Underburden	2600	30.0	0.20

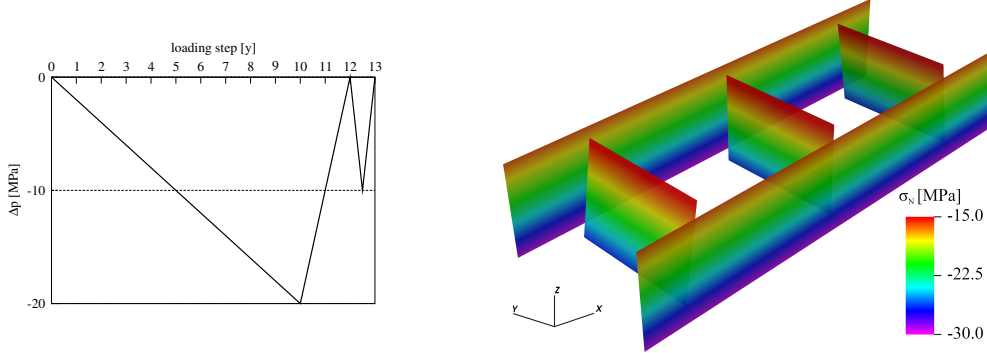


Figure 9: On the left: sketch of the pore pressure variation in time prescribed in an active well of the reservoir compartments. On the right: initial normal stress with respect to the fault orientation. The principal stresses  $\sigma_h$ ,  $\sigma_H$  and  $\sigma_v$  are parallel to the Cartesian axes. Faults F4 and F5 are more loaded because of their orthogonality to  $\sigma_H$ .

period, a 2-year CGI phase follows, where the pressure recovers to the initial (undisturbed) value  $p_i$ , and then UGS cycles start. They are characterized by a 6-month extraction period, during which the pressure drops by 10 MPa, and a 6-month injection period, when the pressure returns to  $p_i$ .

To initialize the simulation, the undisturbed stress regime must be prescribed. We assume it has the principal effective stress tensor directions aligned with the Cartesian axes, in particular,  $\sigma_1 = \sigma_v = \sigma_z$ ,  $\sigma_2 = \sigma_H = \sigma_y$ , and  $\sigma_3 = \sigma_h = \sigma_x$ , where  $\sigma_v$  denotes the vertical compressive stress, and  $\sigma_H$  and  $\sigma_h$  the largest and smallest compressive horizontal principal stress, respectively. At the reservoir average depth, i.e.,  $z = -2100$  m, we have  $\sigma_v = -25.4$  MPa,  $\sigma_h = M_1\sigma_v = -18.8$  MPa,  $\sigma_H = M_2\sigma_v = -21.1$  MPa, with  $M_1 = 0.40$  and  $M_2 = 0.47$ . The initial normal stress acting on the faults is shown in Fig. 9.

Two scenarios have been simulated based on the parameters describing the Coulomb frictional criterion. In the reference scenario (scenario 1)  $\varphi_s = 30^\circ$  and fault weakening is not accounted for. The effect of slip-weakening behavior is investigated in scenario 2, where the friction angle reduces from  $\varphi_s = 30^\circ$  to  $\varphi_d = 10^\circ$  in a slip distance of  $D_c = 2$  mm. Cohesion  $c = 2$  MPa in both scenarios. Finally, the time step is 1 year during the PP phase, then during CGI and UGS phases it is reduced to 2 months.

#### 4. Numerical results

The objective of the representative simulations reported herein is to evaluate the fault reactivation risk during the different stages of the UGS activities in the conceptual reservoir. For this reason, we mainly focus on the criticality index  $\chi$  defined in Eq. (25). For the sake of clarity and ease of readability,  $\chi$  is represented for each fault as a function of depth only, i.e., for each  $z$ -value we compute the  $\chi$  average for the stripe of interface elements located at the same depth. Another significant quantity is the maximum sliding, i.e., the maximum value of  $\|g_T\|_2$  simulated along each fault. These two quantities are closely related each other, since a single element can slide only when  $\chi = 1$ . However, we prefer to propose an averaged version of  $\chi$ , so as to obtain information on the criticality state of the entire fracture at a given depth.

The last quantity used to interpret the results and analyze the fault behavior is the tangential component of the traction. In particular, we use  $t_{T,z}$ , i.e., the vertical component of  $t_T$ . Usually, the 2-norm of the tangential traction is

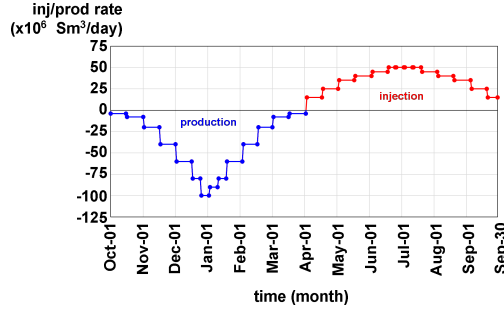


Figure 10: Time behavior of the production/injection rate used in the OPM simulation.

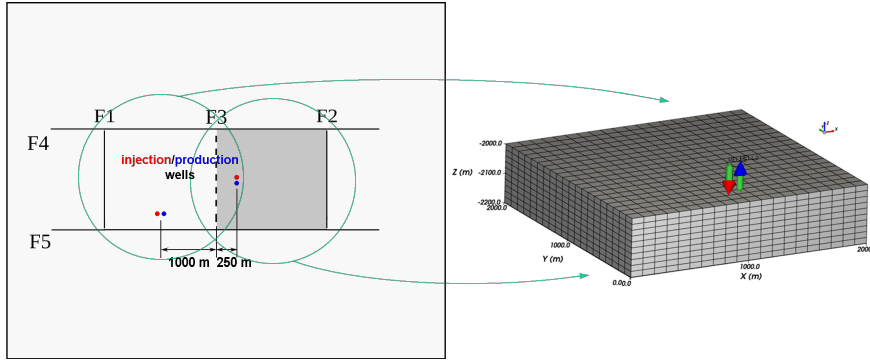


Figure 11: Location of the injection/production wells in the two reservoir blocks (left) and axonometric view of the 3D computational grid used in OPM to simulate the injection/production phase in each reservoir compartment (right). The OPM mesh exactly corresponds to the finite element grid of a single block within the 3D geomechanical model.

analyzed, i.e.,  $\|\mathbf{t}_T\|_2$ , but this does not provide information on the shear direction. However, thanks to the symmetric geometry of the conceptual model, in some locations there is no horizontal component of  $\mathbf{t}_T$ , thus,  $\|\mathbf{t}_T\|_2 = |t_{T,z}|$ . The two quantities share the same modulus, but the vertical component carries additional information on the sliding direction.

#### 4.1. Pore pressure variation

As previously mentioned, in this work we adopt a one-way coupled approach, thus the multiphase flow prediction is computed first. The simulation is performed through the open-source reservoir simulator Open Porous Media [74, 75]. As a reference scenario, a typical year-long cycle of UGS activity has been considered, with the injection-production history represented in Fig. 10. Fig. 11 shows the location of the injection/production wells with respect to the fault system. Note that, to avoid any interpolation among computational grids, the OPM finite volume mesh exactly corresponds to the finite element grid of a single block within the 3D geomechanical model. The characteristic horizontal and vertical permeability of a reservoir in the study area are  $k_h = 600$  mD and  $k_v = 300$  mD, respectively. The “working gas” volume amounts to  $6.5 \times 10^9$  Sm<sup>3</sup> per compartment.

The numerical results in terms of pressure variation are summarized in Fig. 12. The figure shows the depth-averaged pressure behavior along a section passing through the production/injection wells every 3 months. After 3 months the maximum production rate is achieved, after 6 months the production phase ends, after 9 months the maximum injection rate is met, and, finally, after 12 months the simulation ends. Notice that the pressure perturbation during the entire production (or injection) phase is almost uniform in space and varies approximately within the interval between 0 and -10 MPa with respect to the initial value  $p_i$ . This outcome shows that, for the setting defined in these representative simulations, the spatial gradient of the pore pressure variation into each compartment is expected to be quite limited. Hence, considering a constant pressure variation value for each reservoir block appears also to be a reasonable assumption.

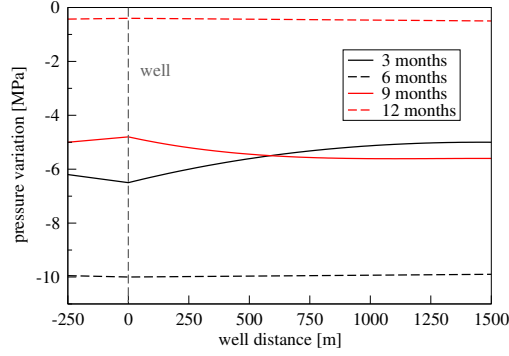


Figure 12: Depth-averaged value of the pore pressure variation during a production/injection cycle as obtained by the OPM flow simulator.

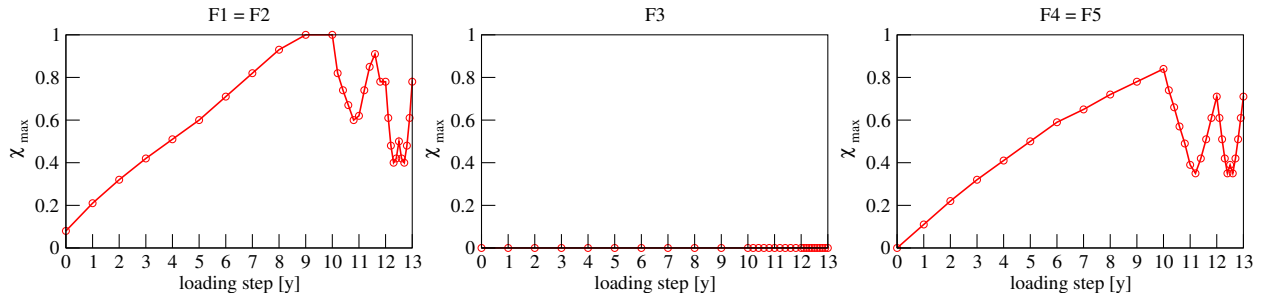


Figure 13: Behavior of  $\chi_{\max}$  from all the loading steps for each fault. Note that due to symmetry F1 and F2 behave identically, as well as F4 and F5.

#### 4.2. Analysis of the fault reactivation risk

The mechanisms for the possible fault reactivation have been investigated in scenario 1. The value  $\chi_{\max} = 1$  is reached on faults F1 and F2 at loading step 9, with  $\chi_{\max}$  up to 0.8 at the end of CG and UGS injection phases (Fig. 13). Conversely,  $\chi = 0$  on fault F3 irrespective of the loading step due to the symmetry of the geometry and loading configurations. A comparison between the behavior versus depth of the criticality index along fault F1 and F4 and the distribution of  $\chi$  on the whole fault system at the end of PP are shown in Fig. 14. Notice that the most critical condition develops along the top and bottom of the reservoir in agreement with previous modeling study [35]. Moreover, faults F4 and F5 exhibit smaller values of  $\chi$  with respect to F1 and F2, showing that a sub-vertical orientation is usually more likely to reactivate.

Fig. 15 shows the stress path in the  $t_N - \|\mathbf{t}_T\|_2$  plane experienced by a representative element located on fault F1 at the top of the reservoir. The actual stress state touches the yield bound at loading step number 9 and remains on the yield surface till the end of PP (loading step 10). During CGI, the stress state initially departs from the yield condition but returns close to it during the last part of the injection when the pressure recovers to the initial value. UGS behaves elastically over a new path with respect to what experienced during the last part of the CGI phase, with an almost constant  $t_N$  value. Again, the stress state approaches the critical condition at the end of the UGS injection phase when  $p$  rises back to  $p_i$ .

A deeper explanation for this behavior can be found by analyzing the actual direction of the shear stress. Fig. 16 shows the vertical component of tangential traction  $t_{T,z}$  on fault F1 at loading steps 0 (initial condition), 10, 11, 12, 12.5, and 13. This component is meaningful because of the symmetry of the model, indeed, we have that  $\|\mathbf{t}_T\|_2 = |t_{T,z}|$ . Sketches of the reservoir-fault-sideburden conditions are provided for the same loading steps. The initial shear stress differs from the null value because of the fault dip. The largest value of  $t_{T,z}$  are observed at the end of PP (loading step 10). Reservoir compaction induced by the pressure depletion is accompanied by fault reactivation. Note that a positive and negative shear stress characterizes the reservoir bottom and top, respectively. As physically expected because of the compaction mechanism, the direction of the shear stress is oriented toward the center of the reservoir. When CGI starts, the shear stress orientation changes and the reactivated part of the fault returns stick. At loading

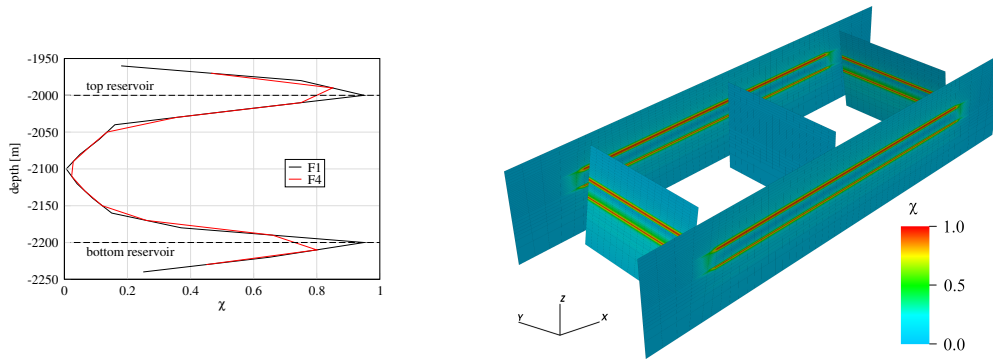


Figure 14: On the left: behavior of the criticality index  $\chi$  vs depth at loading step 10 (end of PP) for faults F1 and F4. On the right:  $\chi$  factor on all the fracture surfaces at loading step 10.

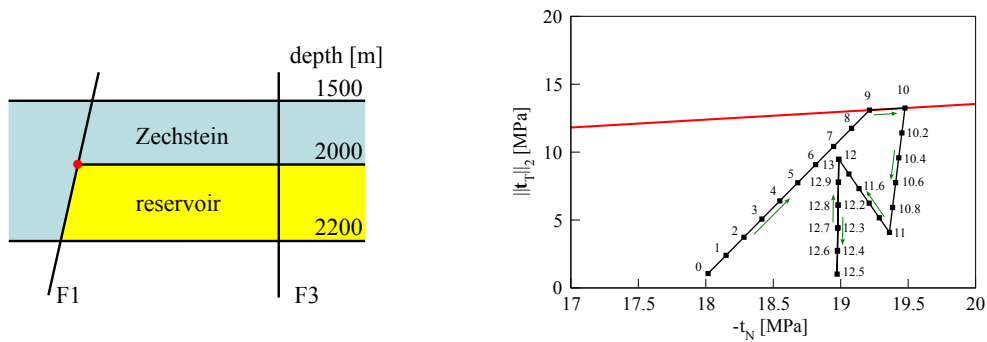


Figure 15: On the left: location of the selected element. On the right: stress path  $\|t_T\|_2$  vs  $-t_N$  for the element highlighted on the left sketch by a red dot. The red line is the yield bound. Numbers along the path denote the loading steps. It can be easily recognized the primary production (loading steps 1 to 10), the cushion gas injection (loading steps 10 to 12) and the underground gas storage (loading steps 12 to 12.5 – production – and 12.5 to 13 – injection).

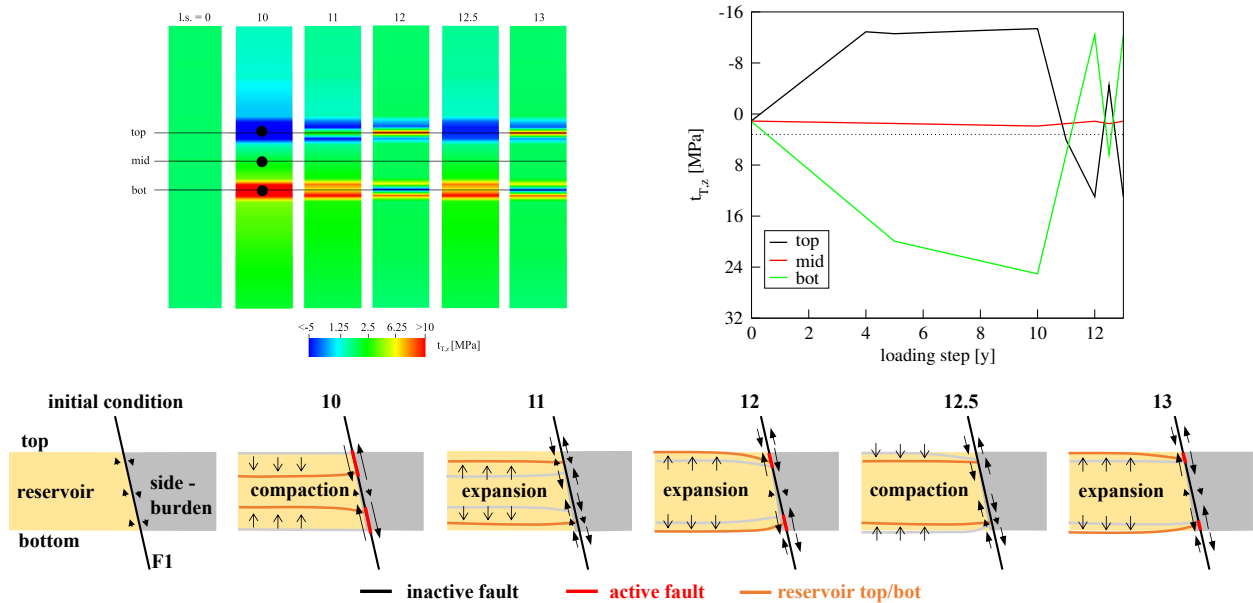


Figure 16: On the top left: distribution of vertical component of the shear stress  $t_{T,z}$  for the loading steps (l.s.) 0 (initial condition), 10, 11, 12, 12.5, 13 on fault F1 (dip =  $10^\circ$ ). On the top right: time behavior of  $\|t_T\|_2$  for the points denoted by the thick black dots in the previous frame located at the top, bottom, and center of the reservoir. Positive values mean that the shear stress is directed upward. On the bottom: sketches representing the reservoir deformation, shear stress direction, and inactive/active portions of the fault at the same loading steps.



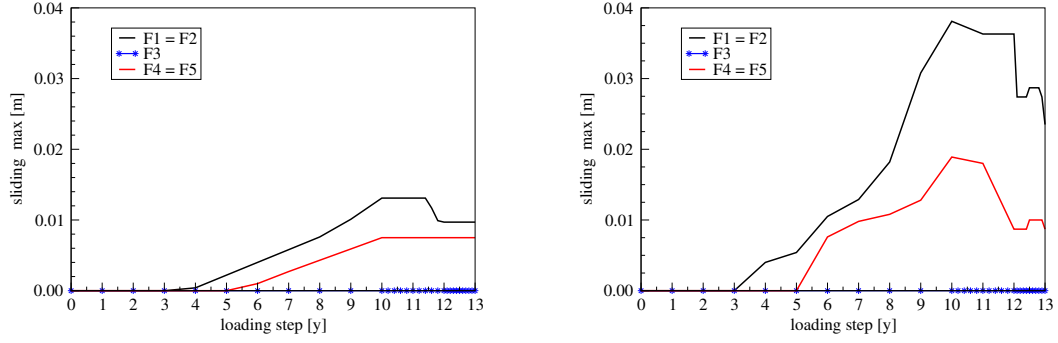


Figure 17: Maximum sliding versus time for the investigated scenarios. On the left: reference case (scenario 1). On the right: using slip-weakening constitutive law (scenario 2).

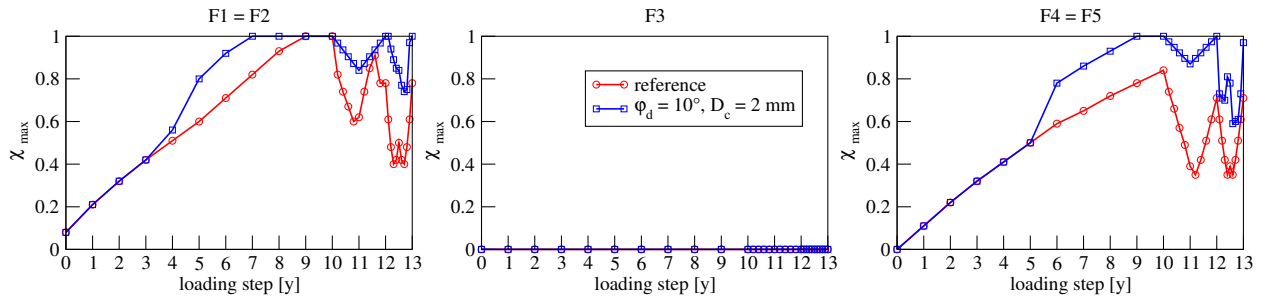


Figure 18: Effect of the Coulomb parameters on  $\chi_{\max}$  at increasing loading steps for each fault. As usual, the pairs F1-F2 and F4-F5 behave identically due to symmetry. The proposed scenario corresponds to  $\varphi_d = 10^\circ$  and  $D_c = 2$  mm.

step 11, half of the pore pressure change has been recovered. As the reservoir expands due to pressure recovery,  $t_{T,z}$  decreases on the reservoir top and bottom (the orientation remains the same but the absolute value decreases) and an almost null  $t_{T,z}$  on the previously sliding IEs is obtained at this step. Differently,  $t_{T,z}$  does not significantly change for the elements surrounding the activated stripes of the fault. The reservoir continues to recover pressure and re-expand until loading step 12. During this second part of CGI shear stress increases, with a sign opposite to that experienced during PP (Fig. 16). A mirror behavior occurs for the IEs at the reservoir bottom. Therefore, expansion during CGI increases the criticality condition of the fault (mainly at the reservoir top and bottom) due the stress re-distribution after the sliding developed over the PP. Fig. 13 shows that faults F1 and F2 approach the criticality state ( $\chi_{\max} > 0.8$ ) when the pressure recover the initial value at the end of CGI and UGS injection phase, i.e., in a pressure state close to the initial undisturbed one, which is not generally expected to be associated to fault reactivation.

#### 4.3. Slip-weakening effect

The adopted Coulomb frictional criterion can handle slip-weakening effects. Here the outcome of a slip-weakening constitutive law for the fault behavior is compared to that previously obtained using a static friction coefficient equal to  $\varphi_s = 30^\circ$ . The two parameters defining the new constitutive law are  $\varphi_d$  and  $D_c$ , i.e., the dynamic friction angle and the slip weakening distance, respectively. In the simulated scenario, the friction angle reduces from  $\varphi_s = 30^\circ$  to  $\varphi_d = 10^\circ$  in a slip distance of  $D_c = 2$  mm.

Fig. 17 provides the time behavior of the fault maximum sliding for the proposed scenario. It can be seen that the current sliding is more than twice that obtained using a static friction angle. Fig. 18 shows a comparison between the criticality index during the entire simulation for scenario 1 and 2. It can be noticed that the new constitutive law causes F1, F2, F4 and F5 to slip as well at the end of the cushion gas and UGS injection phases, but not at loading step 12.5, i.e., at the end of the 6-month UGS production phase (see the zoom in Fig. 19).

Finally, Fig. 20 shows the stress path for the same location as in Fig. 15. Because of the reduced friction angle, the yield surface is reached more easily during PP, at the end of CGI, and at the end of UGS phases. As observed for

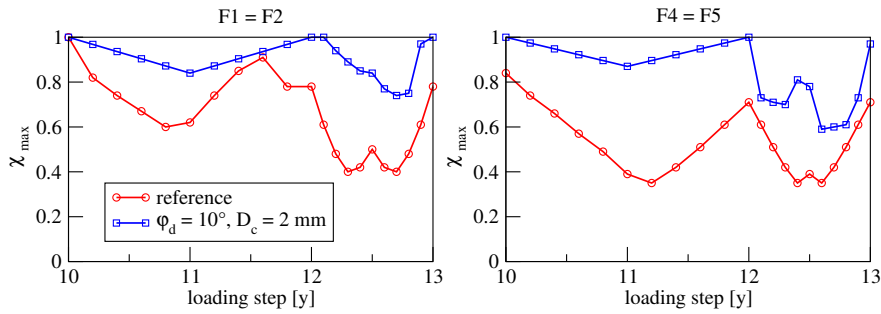


Figure 19: Zoom of Fig. 18 over the cushion gas injection and UGS phases for faults F1 = F2 and F4 = F5.

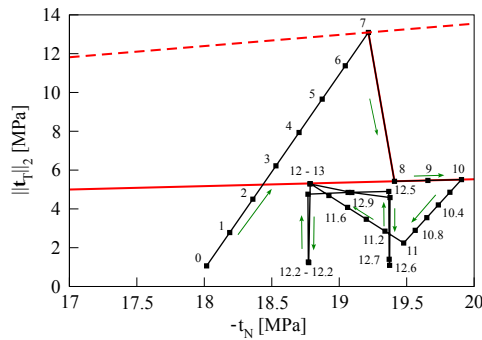


Figure 20: Stress path  $\|t_7\|_2$  vs  $-t_N$  for the F1 element highlighted in Fig. 15. The dashed and the continuous red lines are the yield bound corresponding to the static condition ( $\varphi_s$ ) and after the slip distance  $D_c$  is overcome, respectively. The numbers along the path denote the loading steps. The primary production (loading steps 1 to 10), the cushion gas injection (loading steps 11 to 12) and the underground gas storage (loading steps 12 to 12.5 – production – and 12.5 to 13 – injection) can be easily recognized.

the reference scenario, the elastic phases develop with an almost constant normal stress because of the selected ratios between the reservoir and overburden stiffness and between the pressure change in the reservoir and within the fault. The stress path and the yield bound are quite complex due to weakening. Moreover, due to the very small friction angle ( $\varphi = 10^\circ$ ), a large part of UGS is characterized by a the stress state that develops either on the yield surface or very close to it.

## 5. Conclusions

The first underground gas storage site became operational as early as 1915 [90]. Since then, this technology has spread to all continents, reaching nowadays more than 600 facilities worldwide. Despite this large use, there are risks related to the possible reactivation of existing geological fractures. Although it is a “rare” event from a statistical viewpoint [28], it deserves the proper attention due to its strong social and economic effects. Most of recorded human-induced seismic events can be explained by a pressure increase until it exceeds the initial value, triggering the shear stress on the fault surface to reach the limit strength. However, there are recorded events that cannot be explained by this mechanism. They are the so-called “unexpected” seismic events, which occur when the pressure is in the range already experienced during the primary production. The main scope of this work is to identify these phenomena, explain their basic processes, and define some safe operational bandwidth for the UGS reservoir management with reference to the gas fields located in the Roetligend formation, the Netherlands. To accomplish these aims, we use a computational modeling approach for the accurate and robust simulation of the mechanics of faulted porous rocks.

The overall work is split into two parts. This paper deals with Part I, which concerns the development, implementation and test of the mathematical and numerical model used for computational simulations. A one-way coupled strategy is adopted to deal with the poro-mechanical interaction. First, the set of governing relationships for frictional contact mechanics are introduced, then the weak variational formulation is derived and discretized. We use Lagrange

multipliers to prescribe the normal and frictional constraints on faults, a mixed-dimensional approach, and a mixed finite element discretization with displacement in the 3D porous body and traction on the fault surfaces are the main unknowns. In order to be consistent with classical finite volume discretizations for the multiphase flow, we focus on low-order hexahedral elements for the 3D continuum and a piecewise constant representation of the traction on the contact surfaces, thus requiring a proper stabilization to ensure the regularity of the resulting generalized saddle-point problem. An active-set algorithm and an exact Newton method are implemented for the solution of the overall non-linear problem, while ad hoc preconditioning strategies are used to allow for and accelerate the convergence of the inner linear Krylov solver. A discussion on the slip-weakening constitutive law for fault frictional behavior is also provided. Finally, the model is applied to two realistic scenarios, carried out on a conceptual model built from an idealization of real UGS fields located in the formation of interest. Modeling simulations allow to identify the main mechanisms potentially inducing a fault reactivation during UGS activities, even in “unexpected” situations where the current stress state appears to be less demanding than what the porous medium had already experienced in the past. The use of a slip-weakening rheological model for the frictional behavior can increase the chance of producing a fault reactivation during CGI and UGS activities.

Part II of this work will focus on the model application in a real-world scenario, with an extensive sensitivity analysis on the factors that can mostly impact on the reactivation chances. Further development concerns widening the feasible parameter ranges, e.g., testing different constitutive laws for the continuous medium, using different parameter values, changing the fault positions and orientation. The analysis will be extended to other kinds of storage activities, such as CO<sub>2</sub> geological sequestration or underground H<sub>2</sub> and N<sub>2</sub> storage. The final objective is to draw some guidelines to define a safe operational bandwidth for the management of storage reservoirs in the Netherlands, and, at the same time, build a methodological example that can be successfully extended to other real-world experiences.

### CRediT authorship contribution statement

**Andrea Franceschini:** Methodology, Software, Writing - Original Draft, Visualization. **Claudia Zoccarato:** Conceptualization, Methodology, Formal analysis, Investigation. **Selena Baldan:** Investigation, Visualization. **Matteo Frigo:** Software, Investigation. **Massimiliano Ferronato:** Conceptualization, Methodology, Writing - Review and Editing, Supervision. **Carlo Janna:** Software. **Giovanni Isotton:** Software. **Pietro Teatini:** Conceptualization, Methodology, Formal analysis, Writing - Review and Editing, Supervision, Funding acquisition.

### Declaration of competing interest

The authors declare that they have no known competing financial interests or personal relationships that could have appeared to influence the work reported in this paper.

### Acknowledgements

This research was supported by the State Supervision of Mines (SodM), Ministry of Economic Affairs (The Netherlands), Project KEM01 “Safe Operational Bandwidth of Gas Storage Reservoirs” grant. Portions of this work were performed within the 2020 INdAM-GNCS project “Optimization and advanced linear algebra for PDE-governed problems”. Computational resources were provided by University of Padova Strategic Research Infrastructure Grant 2017: “CAPRI: Calcolo ad Alte Prestazioni per la Ricerca e l’Innovazione”.

### References

- [1] C. Doglioni, A classification of induced seismicity, *Geoscience Frontiers* 9 (2018) 1903–1909. doi:10.1016/j.gsf.2017.11.015.
- [2] G. R. Foulger, M. P. Wilson, J. G. Gluyas, B. R. Julian, R. J. Davies, Global review of human-induced earthquakes, *Earth-Science Reviews* 178 (2018) 438–514. doi:10.1016/j.earscirev.2017.07.008.
- [3] K. M. Keranen, M. Weingarten, Induced Seismicity, *Annual Review of Earth and Planetary Sciences* 46 (2018) 149–174. doi:10.1146/annurev-earth-082517-010054.
- [4] P. Segall, J.-R. Grasso, A. Mossop, Poroelastic stressing and induced seismicity near the Lacq gas field, southwestern France, *Journal of Geophysical Research: Solid Earth* 99 (1994) 15423–15438. doi:10.1029/94jb00989.

- [5] M. H. H. Hettema, P. M. T. M. Schutjens, B. J. M. Verboom, H. J. Gussinklo, Production-Induced Compaction of a Sandstone Reservoir: The Strong Influence of Stress Path, *SPE Reservoir Evaluation & Engineering* 3 (2000) 342–347. doi:10.2118/65410-pa.
- [6] T. Candela, S. Osinga, J.-P. Ampuero, B. Wassing, M. Pluymaekers, P. A. Fokker, J.-D. van Wees, H. A. de Waal, A. G. Muntendam-Bos, Depletion-Induced Seismicity at the Groningen Gas Field: Coulomb Rate-and-State Models Including Differential Compaction Effect, *Journal of Geophysical Research: Solid Earth* 124 (2019) 7081–7104. doi:10.1029/2018jb016670.
- [7] L. Buijze, P. A. van den Bogert, B. B. Wassing, B. Orlic, J. ten Veen, Fault reactivation mechanisms and dynamic rupture modelling of depletion-induced seismic events in a Rotliegend gas reservoir, *Netherlands Journal of Geosciences* 96 (2017) s131–s148. doi:10.1017/njg.2017.27.
- [8] K. W. Chang, P. Segall, Injection-induced seismicity on basement faults including poroelastic stressing, *Journal of Geophysical Research: Solid Earth* 121 (2016) 2708–2726. doi:10.1002/2015jb012561.
- [9] J. Rutqvist, A. P. Rinaldi, F. Cappa, P. Jeanne, A. Mazzoldi, L. Urpi, Y. Guglielmi, V. Vilarrasa, Fault activation and induced seismicity in geological carbon storage - Lessons learned from recent modeling studies, *Journal of Rock Mechanics and Geotechnical Engineering* 8 (2016) 789–804. doi:10.1016/j.jrmge.2016.09.001.
- [10] T. S. Eyre, D. W. Eaton, D. I. Garagash, M. Zecevic, M. Venieri, R. Weir, D. C. Lawton, The role of aseismic slip in hydraulic fracturing-induced seismicity, *Science Advances* 5 (2019). doi:10.1126/sciadv.aav7172.
- [11] Y. Tan, J. Hu, H. Zhang, Y. Chen, J. Qian, Q. Wang, H. Zha, P. Tang, Z. Nie, Hydraulic Fracturing Induced Seismicity in the Southern Sichuan Basin Due to Fluid Diffusion Inferred From Seismic and Injection Data Analysis, *Geophysical Research Letters* 47 (2020) e2019GL084885. doi:10.1029/2019g1084885.
- [12] J. P. Deflandre, J. Laurent, D. Michon, E. Blondin, Microseismic surveying and repeated VSPs for monitoring an underground gas storage reservoir using permanent geophones, *First Break* 13 (2018) 129–138. doi:10.3997/1365-2397.1995008.
- [13] S. Cesca, F. Grigoli, S. Heimann, A. Gonzalez, E. Buforn, S. Maghsoudi, E. Blanch, T. Dahm, The 2013 September–October seismic sequence offshore Spain: a case of seismicity triggered by gas injection?, *Geophysical Journal International* 198 (2014) 941–953. doi:10.1093/gji/ggu172.
- [14] P. Zhou, H. Yang, B. Wang, J. Zhuang, Seismological Investigations of Induced Earthquakes Near the Hutubi Underground Gas Storage Facility, *Journal of Geophysical Research: Solid Earth* 124 (2017) 8753–8770. doi:10.1029/2019jb017360.
- [15] B. H. Hager, M. N. Toksoz, Technical Review of Bergermeer Seismicity Study TNO Report 2008-U-R1071/B, Technical Report, Massachusetts Institute of Technology, 2009.
- [16] D. Kraaijpoel, D. Nieuwland, B. Dost, Microseismic Monitoring and Subseismic Fault Detection in an Underground Gas Storage, in: *Proc. 4th EAGE Passive Seismic Workshop*, Amsterdam, Netherlands, European Association of Geoscientists & Engineers, 2013, pp. 1–3. doi:10.3997/2214-4609.20142354.
- [17] TNO, Injection-Related Induced Seismicity and its Relevance to Nitrogen Injection: Description of Dutch Field Cases, Technical Report, TNO R10906, 2015.
- [18] Nederlandse Aardolie Maatschappij BV, Norg UGS fault reactivation study and implications for seismic threat, Technical Report, Nam Ep201610208045, 2016.
- [19] H. Plaat, Underground gas storage: Why and how, *Geological Society, London, Special Publications* 313 (2009) 25–37. doi:10.1144/sp313.4.
- [20] S. Cornot-Gandolphe, Underground Gas Storage in the World - 2019 Status, Technical Report, CEDIGAZ Insights # 35, 2019.
- [21] B. Zakeri, S. Syri, Electrical energy storage systems: A comparative life cycle cost analysis, *Renewable and Sustainable Energy Reviews* 42 (2015) 569–596. doi:10.1016/j.rser.2014.10.011.
- [22] J. Mouli-Castillo, M. Wilkinson, D. Mignard, C. McDermott, R. S. Haszeldine, Z. K. Shipton, Inter-seasonal compressed-air energy storage using saline aquifers, *Nature Energy* 4 (2019) 131–139. doi:10.1038/s41560-018-0311-0.
- [23] D. Sopher, C. Juhlin, T. Levental, M. Erlström, K. Nilsson, J. P. Da Silva Soares, Evaluation of the subsurface compressed air energy storage (CAES) potential on Gotland, Sweden, *Environmental Earth Sciences* 78 (2019). doi:10.1007/s12665-019-8196-1.
- [24] M. H. Mosleh, M. Sedighi, M. Babaei, M. Turner, Geological sequestration of carbon dioxide, Academic Press, 2019, pp. 487–500. doi:10.1016/B978-0-12-8141104-5.00016-8.
- [25] P. Teatini, N. Castelletto, M. Ferronato, G. Gambolati, C. Janna, E. Cairo, D. Marzorati, D. Colombo, A. Ferretti, A. Bagliani, F. Bottazzi, Geomechanical response to seasonal gas storage in depleted reservoirs: A case study in the Po River basin, Italy, *Journal of Geophysical Research: Earth Surface* 116 (2011). doi:10.1029/2010jf001793.
- [26] European Commission, Questions and Answers on the new EU rules on gas storage, [https://ec.europa.eu/commission/presscorner/detail/en/qanda\\_22\\_1937](https://ec.europa.eu/commission/presscorner/detail/en/qanda_22_1937), 2023. Accessed: 2023-06-28.
- [27] H. Z. Li, P. M. Saint-Vincent, M. Mundia-Howe, N. J. Pekney, A national estimate of US underground natural gas storage incident emissions, *Environmental Research Letters* 17 (2022) 084013. doi:10.1088/1748-9326/ac8069.
- [28] HiQuake, The Human-Induced Earthquake Database, <https://inducedearthquakes.org>, 2023. Accessed: 2023-06-28.
- [29] D. L. Gautier, Carboniferous-Rotliegend Total Petroleum System Description and Assessment Results Summary, Technical Report, U. S. Geological Survey Bulletin 2211, 2003.
- [30] J. van Wees, L. Buijze, K. Thienen-Visser, M. Nepveu, B. Wassing, B. Orlic, P. Fokker, Geomechanics response and induced seismicity during gas field depletion in the Netherlands, *Geothermics* 52 (2014) 206–219. doi:10.1016/j.geothermics.2014.05.004.
- [31] P. Uta, Recent Intraplate Earthquakes in Northwest Germany - Glacial Isostatic Adjustment and/or a Consequence of Hydrocarbon Production, Ph.D. thesis, Leibniz University Hannover, 2017. doi:10.15488/9088.
- [32] K. van Thienen-Visser, J. N. Breunese, Induced seismicity of the Groningen gas field: History and recent developments, *The Leading Edge* 34 (2015) 664–671. doi:10.1190/tle34060664.1.
- [33] J. van Wees, P. A. Fokker, K. Van Thienen-Visser, B. Wassing, S. Osinga, B. Orlic, S. A. Ghouri, L. Buijze, M. Pluymaekers, Geomechanical models for induced seismicity in the Netherlands: inferences from simplified analytical, finite element and rupture model approaches, *Netherlands Journal of Geosciences* 96 (2017) s183–s202. doi:10.1017/njg.2017.38.
- [34] D. Zbinden, A. P. Rinaldi, L. Urpi, S. Wiemer, On the physics-based processes behind production-induced seismicity in natural gas fields,

- Journal of Geophysical Research: Solid Earth 122 (2017) 3792–3812. doi:10.1002/2017jb014003.
- [35] C. Haug, J.-A. Nüchter, A. Henk, Assessment of geological factors potentially affecting production-induced seismicity in North German gas fields, *Geomechanics for Energy and the Environment* 16 (2018) 15–31. doi:10.1016/j.gete.2018.04.002.
- [36] A. Nagelhout, J. Roest, Investigating fault slip in a model of an underground gas storage facility, *International Journal of Rock Mechanics and Mining Sciences* 34 (1997) 212.e1–212.e14. doi:10.1016/s1365-1609(97)00051-8.
- [37] B. Orlic, B. B. T. Wassing, C. R. Geel, Field scale geomechanical modeling for prediction of fault stability during underground gas storage operations in a depleted gas field in the Netherlands, in: *47th US Rock Mechanics / Geomechanics Symposium*, Paper #ARMA 13-300, American Rock Mechanics Association, 2013, pp. 1–11.
- [38] P. Teatini, M. Ferronato, A. Franceschini, M. Frigo, C. Janna, C. Zoccarato, Gas storage in compartmentalized reservoirs: a numerical investigation on possible “unexpected” fault activation, in: *53rd US Rock Mechanics / Geomechanics Symposium*, Paper #ARMA 19-1991, American Rock Mechanics Association, 2019, pp. 1–9.
- [39] P. Teatini, C. Zoccarato, M. Ferronato, A. Franceschini, M. Frigo, C. Janna, G. Isotton, About geomechanical safety for UGS activities in faulted reservoirs, *Proceedings of the International Association of Hydrological Sciences* 382 (2020) 539–545. doi:10.5194/piahs-382-539-2020.
- [40] P. Teatini, S. Baldan, C. Zoccarato, M. Ferronato, A. Franceschini, M. Frigo, C. Janna, G. Isotton, Unexpected fault activation in underground gas storage. Part II: Safe operational bandwidth for reservoirs in the Roetligend formation, the Netherlands., *Geomechanics for Energy and the Environment* (2023) submitted.
- [41] A. Franceschini, M. Ferronato, C. Janna, P. Teatini, A novel Lagrangian approach for the stable numerical simulation of fault and fracture mechanics, *Journal of Computational Physics* 314 (2016) 503–521. doi:10.1016/j.jcp.2016.03.032.
- [42] A. Franceschini, N. Castelletto, M. Ferronato, Block preconditioning for fault/fracture mechanics saddle-point problems, *Computer Methods in Applied Mechanics and Engineering* 344 (2019) 376–401. doi:10.1016/j.cma.2018.09.039.
- [43] G. Isotton, P. Teatini, M. Ferronato, C. Janna, N. Spiezia, S. Mantica, G. Volonte, Robust numerical implementation of a 3D rate-dependent model for reservoir geomechanical simulations, *International Journal for Numerical and Analytical Methods in Geomechanics* 43 (2019) 2752–2771. doi:10.1002/nag.3000.
- [44] G. Gambolati, P. Teatini, D. Baù, M. Ferronato, Importance of poroelastic coupling in dynamically active aquifers of the Po river basin, Italy, *Water Resources Research* 36 (2000) 2443–2459. doi:10.1029/2000wr900127.
- [45] L. Buijze, P. A. J. van den Bogert, B. B. T. Wassing, B. Orlic, Nucleation and Arrest of Dynamic Rupture Induced by Reservoir Depletion, *Journal of Geophysical Research: Solid Earth* 124 (2019) 3620–3645. doi:10.1029/2018JB016941.
- [46] A. Bizzarri, How to promote earthquake ruptures: different nucleation strategies in a dynamic model with slip-weakening function, *Bulletin of the Seismological Society of America* 100 (2010) 923–940. doi:10.1785/0120090179.
- [47] N. Kikuchi, J. T. Oden, *Contact Problems in Elasticity: A Study of Variational Inequalities and Finite Element Methods*, Society for Industrial and Applied Mathematics, Philadelphia, PA, USA, 1988. doi:10.1137/1.9781611970845.
- [48] T. A. Laursen, *Computational Contact and Impact Mechanics: Fundamentals of Modeling Interfacial Phenomena in Nonlinear Finite Element Analysis*, Springer-Verlag Berlin Heidelberg, 2003. doi:10.1007/978-3-662-04864-1.
- [49] P. Wriggers, *Computational Contact Mechanics*, 2nd ed., Springer-Verlag Berlin Heidelberg, 2006. doi:10.1007/978-3-540-32609-0.
- [50] B. Wohlmuth, Variationally consistent discretization schemes and numerical algorithms for contact problems, *Acta Numerica* 20 (2011) 569–734. doi:10.1017/s0962492911000079.
- [51] J. C. Simo, T. J. R. Hughes, *Computational Inelasticity*, Springer-Verlag New York, 1998. doi:10.1007/b98904.
- [52] A. Franceschini, N. Castelletto, J. A. White, H. A. Tchelepi, Algebraically stabilized Lagrange multiplier method for frictional contact mechanics with hydraulically active fractures, *Computer Methods in Applied Mechanics and Engineering* 368 (2020) 113161. doi:10.1016/j.cma.2020.113161.
- [53] A. Franceschini, N. Castelletto, J. A. White, H. A. Tchelepi, Scalable preconditioning for the stabilized contact mechanics problem, *Journal of Computational Physics* 459 (2022) 111150. doi:10.1016/j.jcp.2022.111150.
- [54] O. Coussy, *Poromechanics*, John Wiley & Sons Ltd. Chichester, England, 2004. doi:10.1002/0470092718.
- [55] E. A. De Souza Neto, D. Peric, D. R. Owen, *Computational methods for plasticity: theory and applications*, John Wiley & Sons, 2011. doi:10.1002/9780470694626.
- [56] L. Xikui, O. Zienkiewicz, Multiphase flow in deforming porous media and finite element solutions, *Computers & structures* 45 (1992) 211–227. doi:10.1016/0045-7949(92)90405-0.
- [57] J. Rutqvist, Y.-S. Wu, C.-F. Tsang, G. Bodvarsson, A modeling approach for analysis of coupled multiphase fluid flow, heat transfer, and deformation in fractured porous rock, *International Journal of Rock Mechanics and Mining Sciences* 39 (2002) 429–442. doi:10.1016/s1365-1609(02)00022-9.
- [58] G. Yadigaroglu, G. F. Hewitt, *Introduction to Multiphase Flow. Basic Concepts, Applications and Modelling*, Springer, 2018. doi:10.1007/978-3-319-58718-9.
- [59] A. Wilkins, C. P. Green, J. Ennis-King, An open-source multiphysics simulation code for coupled problems in porous media, *Computers & Geosciences* 154 (2021) 104820. doi:10.1016/j.cageo.2021.104820.
- [60] T. T. Garipov, M. Karimi-Fard, H. A. Tchelepi, Discrete fracture model for coupled flow and geomechanics, *Computational Geosciences* 20 (2016) 149–160. doi:10.1007/s10596-015-9554-z.
- [61] C. Zoccarato, D. Baù, M. Ferronato, G. Gambolati, A. Alzraiee, P. Teatini, Data assimilation of surface displacements to improve geomechanical parameters of gas storage reservoirs, *Journal of Geophysical Research: Solid Earth* 121 (2016) 1441–1461. doi:10.1002/2015jb012090.
- [62] P. Teatini, N. Castelletto, G. Gambolati, 3D geomechanical modeling for CO<sub>2</sub> geological storage in faulted formations. A case study in an offshore northern Adriatic reservoir, Italy, *International Journal of Greenhouse Gas Control* 22 (2014) 63–76. doi:10.1016/j.ijggc.2013.12.021.
- [63] N. Castelletto, G. Gambolati, P. Teatini, Geological CO<sub>2</sub> sequestration in multi-compartment reservoirs: Geomechanical challenges, *Journal of Geophysical Research: Solid Earth* 118 (2013) 2417–2428. doi:10.1002/jgrb.50180.
- [64] N. Castelletto, M. Ferronato, G. Gambolati, C. Janna, P. Teatini, Compartmentalization Effects in Geologic CO<sub>2</sub> Sequestration. A case Study

- in an Offshore Reservoir in Italy, in: *Poromechanics V: Proceedings of the Fifth Biot Conference on Poromechanics*, 2013, pp. 1265–1270. doi:10.1061/9780784412992.151.
- [65] N. Castelletto, P. Teatini, G. Gambolati, D. Bossie-Codreanu, O. Vincké, J.-M. Daniel, A. Battistelli, M. Marcolini, F. Donda, V. Volpi, Multiphysics modeling of CO<sub>2</sub> sequestration in a faulted saline formation in Italy, *Advances in water resources* 62 (2013) 570–587. doi:10.1016/j.advwatres.2013.04.006.
- [66] R. Eymard, T. Gallouët, R. Herbin, Finite volume methods, *Handbook of numerical analysis* 7 (2000) 713–1018. doi:10.1016/S1570-8659(00)07005-8.
- [67] G. Manzini, A. Russo, A finite volume method for advection–diffusion problems in convection-dominated regimes, *Computer Methods in Applied Mechanics and Engineering* 197 (2008) 1242–1261. doi:10.1016/j.cma.2007.11.014.
- [68] J. Droniou, Finite volume schemes for diffusion equations: introduction to and review of modern methods, *Mathematical Models and Methods in Applied Sciences* 24 (2014) 1575–1619. doi:10.1142/S0218202514400041.
- [69] J. Wan, L. Durlofsky, T. Hughes, K. Aziz, Stabilized finite element methods for coupled geomechanics-reservoir flow simulations, in: *SPE Reservoir Simulation Symposium*, 2003, pp. 1–11. doi:10.2118/79694-MS.
- [70] B. Jha, R. Juanes, A locally conservative finite element framework for the simulation of coupled flow and reservoir geomechanics, *Acta Geotechnica* 2 (2007) 139–153. doi:10.1007/s11440-007-0033-0.
- [71] J. H. Prevost, N. Sukumar, Faults simulations for three-dimensional reservoir-geomechanical models with the extended finite element method, *Journal of the Mechanics and Physics of Solids* 86 (2016) 1–18. doi:10.1016/j.jmps.2015.09.014.
- [72] A. S. Abushaikh, D. V. Voskov, H. A. Tchalepi, Fully implicit mixed-hybrid finite-element discretization for general purpose subsurface reservoir simulation, *J. Comput. Phys.* 346 (2017) 514–538. doi:10.1016/j.jcp.2017.06.034.
- [73] S. Nardean, M. Ferronato, A. Abushaikh, Block constrained pressure residual preconditioning for two-phase flow in porous media by mixed hybrid finite elements, *Computational Geosciences* (2023). doi:10.1007/s10596-023-10238-x.
- [74] The Open Porous Media Initiative, Open Porous Media, <https://opm-project.org>, 2023. Accessed: 2023-07-21.
- [75] A. F. Rasmussen, T. H. Sandve, K. Bao, A. Lauser, J. Hove, B. Skafestad, R. Klöfkorn, M. Blatt, A. B. Rustad, O. Sævareid, K.-A. Lie, A. Thune, The open porous media flow reservoir simulator, *Computers & Mathematics with Applications* 81 (2021) 159–185. doi:10.1016/j.camwa.2020.05.014.
- [76] M. Ferronato, C. Janna, G. Pini, Parallel solution to ill-conditioned FE geomechanical problems, *International Journal for Numerical and Analytical Methods in Geomechanics* 36 (2012) 422–437. doi:10.1002/nag.1012.
- [77] J. Nocedal, S. Wright, *Numerical optimization*, Springer Science & Business Media, 2006. doi:10.1007/b98874.
- [78] H. Antil, D. P. Kouri, M.-D. Lacasse, D. Ridzal, *Frontiers in PDE-constrained Optimization*, volume 163, Springer, 2018. doi:10.1007/978-1-4939-8636-1.
- [79] R. E. Goodman, R. L. Taylor, T. L. Brekke, A model for the mechanics of jointed rock, *Journal of Soil Mechanics & Foundations Div.* 94 (1968) 637–659.
- [80] H. C. Elman, D. J. Silvester, A. J. Wathen, *Finite Elements and Fast Iterative Solvers with Applications in Incompressible Fluid Dynamics*, Oxford University Press, USA, 2014. doi:10.1093/acprof:oso/9780199678792.001.0001.
- [81] The Atlas Project Team, Atlas web page, <https://www.m3eweb.it/atlas>, 2023. URL: <https://www.m3eweb.it/atlas>.
- [82] M. Benzi, G. H. Golub, J. Liesen, Numerical solution of saddle point problems, *Acta Numerica* 14 (2005) 1–137. doi:10.1017/s0962492904000212.
- [83] A. Franceschini, M. Ferronato, M. Frigo, C. Janna, A reverse augmented constraint preconditioner for Lagrange multiplier methods in contact mechanics, *Computer Methods in Applied Mechanics and Engineering* 392 (2022) 114632. doi:10.1016/j.cma.2022.114632.
- [84] D. J. Andrews, Rupture velocity of plane strain shear cracks, *Journal of Geophysical Research* 81 (1976) 5679–5687. doi:10.1029/JB081i032p05679.
- [85] Y. Ida, Cohesive force across the tip of a longitudinal-shear crack and Griffith’s specific surface energy, *Journal of Geophysical Research* 77 (1972) 3796–3805. doi:10.1029/JB077i020p03796.
- [86] A. C. Palmer, J. R. Rice, The growth of slip surfaces in the progressive failure of over-consolidated clay, *Proceedings of the Royal Society of London. A. Mathematical and Physical Sciences* 332 (1973) 527–548. doi:10.1098/rspa.1973.0040.
- [87] L. B. Hunfeld, J. Chen, S. Hol, A. R. Niemeijer, C. J. Spiers, Healing Behavior of Simulated Fault Gouges From the Groningen Gas Field and Implications for Induced Fault Reactivation, *Journal of Geophysical Research: Solid Earth* 125 (2020) e2019JB018790. doi:10.1029/2019JB018790.
- [88] P. Fokker, B. Wassing, F. Van Leijen, R. Hanssen, D. Nieuwland, Data assimilation of PS-InSAR movement measurements applied to the Bergrmeer gas field, in: *International EAGE Workshop on Geomechanics and Energy*, 2013, pp. cp-369. doi:10.3997/2214-4609.20131971.
- [89] B. Wassing, L. Buijze, J. Ter Heege, B. Orlic, S. Osinga, The impact of viscoelastic caprock on fault reactivation and fault rupture in producing gas fields, in: *51st US Rock Mechanics/Geomechanics Symposium*, 2017, pp. 1–13.
- [90] H. Plaat, Underground gas storage: Why and how, *Geological Society, London, Special Publications* 313 (2009) 25–37. doi:10.1144/SP313.4.